Draft version February 2, 2022
Typeset using LaTeX **twocolumn** style in AASTeX63

A Comparison of Rest-frame Ultraviolet and Optical Emission-Line Diagnostics in the Lensed Galaxy SDSS J1723+3411 at Redshift $z = 1.3293$

J. R. Rigby,[1] Michael Florian,[1,*] A. Acharyya,[2] Matthew Bayliss,[3] Michael D. Gladders,[4] Keren Sharon,[5] Gabriel Brammer,[6] Ivelina Momcheva,[7] Stephanie LaMassa,[7] Fuyan Bian,[8] Håkon Dahle,[9] Traci Johnson,[10] Lisa Kewley,[2] Katherine Murray,[7] Katherine Whitaker,[11] and Eva Wuyts[12]

[1] *Observational Cosmology Lab, NASA Goddard Space Flight Center, Code 665, Greenbelt MD 20771, USA*
[2] *The Australian National University, Australia*
[3] *Department of Physics, University of Cincinnati, Cincinnati, OH 45221, USA*
[4] *Department of Astronomy & Astrophysics, The University of Chicago, 5640 S. Ellis Avenue, Chicago, IL 60637, USA*
[5] *University of Michigan, Department of Astronomy, 1085 South University Avenue, Ann Arbor, MI 48109, USA*
[6] *The Cosmic Dawn Center, University of Copenhagen, Denmark*
[7] *Space Telescope Science Institute, 3700 San Martin Dr., Baltimore, MD 21218, USA*
[8] *European Southern Observatory, Alonso de Córdova 3107, Casilla 19001, Vitacura, Santiago 19, Chile*
[9] *Institute of Theoretical Astrophysics, University of Oslo, P.O. Box 1029, Blindern, NO-0315 Oslo, Norway*
[10] *Enterprise Analytics, CVS Health, 2211 Sanders Rd, Northbrook IL 60062, USA*
[11] *Department of Astronomy, University of Massachusetts Amherst, 710 N Pleasant Street, Amherst, MA 01003, USA*
[12] *ArmenTeKort, Antwerp, Belgium*

(Received 19 June 2020; Accepted 5 October 2020; ApJ in press)

ABSTRACT

For the extremely bright lensed galaxy SDSS J1723+3411 at $z = 1.3293$, we analyze spatially integrated MMT, Keck, and *Hubble Space Telescope* spectra that fully cover the rest-frame wavelength range of 1400 Å to 7200 Å. We also analyze near-IR spectra from Gemini that cover Hα for a portion of the lensed arc. We report fluxes for 42 detected emission lines, and upper limits for an additional 22. This galaxy has extreme emission line ratios and high equivalent widths that are characteristic of extreme emission-line galaxies. We compute strong emission line diagnostics from both the rest-frame optical and rest-frame ultraviolet (UV), to constrain physical conditions and test the spectral diagnostics themselves. We tightly determine the nebular physical conditions using the most reliable diagnostics, and then compare to results from other diagnostics. We find disappointing performance from the UV–only diagnostics: they either are unable to measure the metallicity or dramatically underestimate it; they over-estimate the pressure; and the UV diagnostic of ionization parameter has a strong metallicity dependence in this regime. Based on these results, we suggest that upcoming *James Webb Space Telescope* (*JWST*) spectroscopic surveys of galaxies in the reionization epoch should invest the additional integration time to capture the optical [O II] and [O III] emission lines, and not rely solely on the rest-frame UV emission lines. We make available the spectra; they represent one of the highest-quality emission line spectral atlases of star-forming galaxy available beyond the local universe, and will aid planning observations with *JWST*.

Keywords: galaxies: high-redshift—galaxies: evolution—gravitational lensing

1. INTRODUCTION

Nebular emission lines arise from the gas ionized by massive stars, and as such, are a fundamental way by which we understand the physical conditions within galaxies. Spectral diagnostics composed of the fluxes of two or more of these emission lines are used to measure nebular physical conditions, namely the gas pressure, the ionization parameter (defined as the ratio of ionizing photons to electrons), metallicity (expressed as the oxygen abundance relative to hydrogen, defined in

Jane.Rigby@nasa.gov

* NASA Postdoctoral Program Fellow

units of $\log(O/H) + 12$) , and the elemental abundance pattern.

While galaxies produce emission lines over much of the electromagnetic spectrum, the most heavily utilized spectral diagnostics have been in the rest-frame optical, in part because these diagnostics are accessible to ground-based telescopes and have therefore been the workhorses of large, multiplexed spectroscopic surveys. Indeed, the multi-object spectroscopy mode of the NIRSpec instrument on the upcoming *James Webb Space Telescope* (*JWST*) is designed to multiplexedly capture these rest-frame optical diagnostics in galaxies across much of cosmic time, out to very high redshift.

The rest-frame ultraviolet (UV) also features a number of emission lines (Kinney et al. 1993) that are useful as spectral diagnostics (Garnett et al. 1997b,a). Historically, sample sizes at low redshift have been limited due to the difficulty of detecting UV photons. Since the redder of these diagnostic emission lines will redshift out of NIRSpec's range for very high redshift galaxies, multiple groups have been calibrating rest–frame UV emission lines as alternative diagnostics (Bayliss et al. 2014; Stark et al. 2014; Berg et al. 2016; Feltre et al. 2016; Jaskot & Ravindranath 2016; Steidel et al. 2016; Senchyna et al. 2017; Stark et al. 2016; Stroe et al. 2017a,b; Berg et al. 2018; Byler et al. 2018; Nakajima et al. 2018; Shibuya et al. 2018; Kewley et al. 2019b; Berg et al. 2019a,b; Acharyya et al. 2019; Byler et al. 2020), with small sample sizes. These rest-frame UV line diagnostics are promising, but as yet have received a small fraction of the observational and theoretical attention paid to the rest-frame optical lines.

The rest-frame optical diagnostics are either calibrated empirically from H II regions at $z = 0$, or from theoretical models; these various calibrations disagree by up to a factor of five in the local universe (Kewley & Ellison 2008). Furthermore, the rest-frame optical emission line ratios of galaxies have evolved systematically with time (Shapley et al. 2005; Kriek et al. 2007; Brinchmann et al. 2008; Hainline et al. 2009; Kewley et al. 2013b; Steidel et al. 2014; Shapley et al. 2015). The emission line ratios O32[1] and [O III]/Hβ, which are sensitive to ionization parameter, are observed to rise from z=0 to z=0.6 (Kewley et al. 2015), and are elevated in z∼3 galaxies (Holden et al. 2016; Onodera et al. 2016). One proposed explanation for this observed redshift evolution in line ratios is that the ionization parameter evolves, driven by higher specific star formation rates and/or star formation surface densities (Kewley et al. 2015; Hirschmann et al. 2017; Kaasinen et al. 2018; Bian et al. 2016).

It is thus timely to compare these spectral diagnostics of physical conditions of galaxies *in situ* at redshifts $z > 1$, where diagnostic line ratios are known to be elevated. It is especially important to obtain the full suite of diagnostics, both rest-frame UV and rest-frame optical, in order to understand any systematic biases. Observationally this has been difficult due to the faintness of typical galaxies at these redshifts, and due to the Earth's atmospheric opacity that prevents full wavelength coverage in the rest-frame optical (observed-frame near infrared).

A small number of papers have attempted joint analyses of the UV and optical emission lines of galaxies. Steidel et al. (2016) compared the stacked rest-frame UV spectra of 30 galaxies at $z \sim 2.4$ to their stacked rest-frame optical spectra, finding that the UV stellar continuum implied systematically lower metallicities, and attributing this to an atomic abundance pattern with a much higher than solar ratio of alpha-process elements to iron-peak elements. The rest-frame UV emission lines were used to estimate the oxygen abundance via the direct method, using the [O III] (1661 + 1666 Å)/[O III] 5007 Å ratio. Byler et al. (2018) suggested the use of several other rest-frame UV emission lines as spectral diagnostics; Byler et al. (2020) tests the effectiveness of these diagnostics using spectra of local and lensed $z \sim 2$ galaxies.

The most in-depth intercomparison of the rest-frame UV and optical emission lines to date has been carried out by Acharyya et al. (2019), hereafter A19; they jointly analyzed the full suite of rest-frame UV and rest-frame optical emission lines in a single star-forming region within the $z = 1.70$ lensed galaxy RCSGA 032727−132609, using spectra from Rigby et al. (2011) and Rigby et al. (2018). A19 explored how what is inferred depends on what is measured—how the physical constraints depend on whether the input spectra is the UV alone, the optical alone, or the full suite of rest-frame UV and optical lines. Using only the rest-frame UV lines, they were able to constrain the ionization parameter but not the nebular metallicity. They also inferred systematically higher pressures from the rest-frame UV diagnostics compared to the rest-frame optical diagnostics.

A limitation encountered by A19 was the difficulty of relative flux calibration (or "fluxing") across the broad wavelength range of the spectral diagnostics, for two reasons. First, there was a wavelength coverage gap between the rest-frame UV and rest-optical spectra. Second, the near-IR spectra were obtained sequentially in

[1] O32 ≡ [O III] 5007 Å / [O II] 3727, 3729 Å

the three filters (J, H, and K), as the seeing and pointing varied. While the Balmer line ratios were used to scale the relative fluxing across the three near-IR bands, relative fluxing across multiple spectra remained the main source of systematic error in that work.

Even at $z \sim 0$, few galaxies have continuous spectral coverage of rest-frame 1000–7000 Å, due to the difficulty of observing in the UV. Therefore, 1) to prepare for the sorts of datasets that *JWST* will soon obtain for galaxies at higher redshift, 2) to evaluate the performance of the rest-frame UV and the rest-frame optical spectral diagnostics, and 3) to fully constrain the physical conditions of a distant star-forming galaxy, we have obtained new spectra for a lensed galaxy at $z = 1.3293$ that completely cover this rest-frame wavelength range.

In this paper, for the bright gravitationally–lensed giant arc SDSS J1723+3411 at $z = 1.3293$ (Figure 1), we analyze spectra from instruments on four telescopes: the Blue Channel spectrograph on the MMT, the Echellette Spectrograph and Imager (ESI) on the Keck II telescope, the WFC3-IR G102 and G141 grisms onboard the *Hubble Space Telescope* (*HST*), and the Gemini Near-Infrared Spectrograph (GNIRS) on the Gemini-North telescope. All but the Gemini/GNIRS spectra are spatially integrated over the giant arc; the Gemini/GNIRS spectrum covers a small portion of the arc. See Figure 2. We stitch together these spectra to completely cover all rest-frame wavelengths from 1375 to 7230 Å. We publish these spectra, and report fluxes for 42 detected emission lines and upper limits for 22 more emission lines. We believe this to be the most comprehensive set of of emission lines yet published for a galaxy beyond the local universe. From these emission line fluxes, we compute strong emission line diagnostics from both the rest-frame optical and rest-frame UV, in order to constrain the physical conditions of this galaxy, and to test the spectral diagnostics themselves.

2. METHODS

All spectra were corrected for foreground reddening from the Milky Way galaxy, using the value of $E(B-V) = 0.03415$ measured by Green et al. (2015).[2] All spectra have had the barycentric correction applied, and all wavelengths are listed in vacuum. Rest wavelengths are from NIST.[3]

We use a solar oxygen abundance of $12 + \log(O/H) = 8.72$ (Asplund et al. 2009).

[2] Queried using the python interface at http://argonaut.skymaps.info

[3] http://www.pa.uky.edu/%7Epeter/atomic/

We use the convention that negative equivalent width indicates emission, and positive equivalent width indicates absorption.

To convert apparent magnitude to absolute, we assume a ΛCDM cosmology with $\Omega_M = 0.3$, $\Omega_\Lambda = 0.7$, and $h_0 = 70$ km s^{-1} Mpc^{-1}.

2.1. *Target and experimental design*

The galaxy SDSS J1723+3411, a gravitationally lensed giant arc at $z = 1.3293$, was independently discovered by multiple groups from Sloan Digital Sky Survey (SDSS) data. Kubo et al. (2010) reported a redshift for the lensing cluster of $z = 0.4435 \pm 0.0002$, and a redshift for the giant arc of $z = 1.3294 \pm 0.0002$, as measured with the DIS spectrograph on the Apache Point 3.5 m telescope. The CASSOWARY team (Stark et al. 2013) independently found the arc, reporting a lens redshift of $z = 0.444$ and an arc redshift of $z = 1.328$, from spectroscopy with the Blue Channel and Red Channel spectrographs on the MMT. The arc was also independently selected by the Sloan Giant Arcs Survey (SGAS1) (Gladders et al. in prep.) It was first observed by our collaboration in the follow-up imaging program for SGAS candidate lenses at the 2.56 m Nordic Optical Telescope, where we obtained 2x300s g-band exposures with the MOSaic CAmera (MOSCA) on UT date 2010-03-13, in 0.77″ seeing. An updated cluster redshift of $z = 0.44227 \pm 0.00009$ was reported by Sharon et al. (2020), using the SDSS DR12 spectrum of the brightest cluster galaxy.

We chose this lensed galaxy for this experiment because its redshift puts all the rest-frame optical spectral diagnostics within reach of the WFC3-IR grism spectroscopy mode *HST*, and all of the rest-frame UV diagnostics within reach of ground-based telescopes. Further, this redshift places a bright emission line or pair of lines into each region of spectral overlap: the [C III] 1907, C III] 1909 Å doublet is covered by both the MMT and Keck spectra; the [O II] 3727, 3729 Å is covered by both the Keck spectrum and the WFC3-IR G102 grism; and Hβ is covered by both WFC3-IR grisms. This spectral overlap enables the combined spectral dataset to be relatively flux calibrated across the full wavelength range.

2.2. *Lens model*

The lens model for SDSS J1723+3411 is described in Sharon et al. (2020). The cluster lenses SDSS J1723+3411 into a classic five-image lensing configuration, with two merging images straddling the critical curve to form a highly magnified giant arc southeast of the BCG, a counter image north of the BCG, and

two radial images west of the BCG. Sharon et al. (2020) identify a second lensed source at $z = 2.165$, with four images, which are also used to constrain the lens model.

The lens model yields a total magnification for the giant arc of $52.7^{+3.3}_{-1.2}$ (Florian et al. submitted) In general, uncertainty in lensing magnification propagates directly to absolute quantities like stellar mass and luminosity. However, since gravitational lensing is achromatic, the magnification uncertainty has no effect on quantities derived from flux ratios. Thus, the physical conditions inferred later in this work are not affected by the lens model. What is true is that certain portions of the arc are more highly magnified than others, and thus, are over-represented in the spatially-integrated spectrum analyzed in this paper. This is an inevitable issue in lensing, that we must bear in mind when interpreting results from the integrated spectrum. Florian et al. (submitted) analyzes the spatial variation in the line ratios across physically distinct regions of the lensed galaxy, and discusses to what extent this affects the values inferred from integrated spectra. To summarize, for SDSS J1723+3411, the line ratio with the most spatial variation (0.15 dex) is O32. R23 varies by 0.1 dex, and Ne3O2 does not vary significantly. From MAPPINGS-V model grids, this spatial variation in line ratios can be explained by a spread of ~ 0.25 dex in ionization parameter, and a spread in metallicity of 0.3 dex (if on the high metallicity branch, which we think most likely) or zero dex (if on the low metallicity branch.)

2.3. *Observations and Data Reduction*

2.3.1. *HST imaging data*

We obtained imaging of SDSS J1723+3411 with the UVIS and IR channels of the WFC3 instrument (MacKenty 2012) onboard *HST* through guest observer program #13003 (PI Gladders), which was a large program targeting lensed arcs selected by SGAS (Sharon et al. 2020) . The filters used were F390W, F775W, F1110W, and F160W, at depths of 2368 s, 2380 s, 1112 s, and 1112 s respectively. Figure 1 shows a color composite *HST* image of SDSS J1723+3411. The giant arc of SDSS J1723+3411 is labeled as "A1" and "A2" in Figure 1 and in Sharon et al. (2020) . The spectroscopy presented in this paper covers this giant arc. *HST* grism spectra were obtained for additional lensed images of the galaxy, labeled A3, and A4, that are not discussed in this paper.

Additional WFC3-IR imagery was also obtained in the F105W and F140W filters through guest observer program #14230 (PI Rigby), as the non-dispersed images used for wavelength calibration.

2.3.2. *HST WFC3-IR grism spectra*

We obtained spectra of SDSS J1723+3411 with the WFC3 instrument onboard *HST*, using the IR channel and the G102 and G141 grisms, in guest observer program #14230 (PI Rigby). Eight orbits of grism spectroscopy were obtained on UT dates 2016-01-18, 2016-01-19, 2016-07-11, and 2016-07-14. The total integration times were 2.76 hr in each of the G102 and G141 grisms. Direct images for wavelength calibration were obtained using the F105W and F140W filters. The grism observing strategy followed that developed for 3D-HST (Brammer et al. 2012), namely the use of 2x2 interlacing and their four-point dither pattern. Observations were obtained at two different roll angles ("ORIENT" in the *HST* nomenclature) of 139° and 308°. From the range allowed by spacecraft safety constraints, these orientations were chosen such that light was dispersed perpendicular to the length of the arc, while minimizing contamination from cluster galaxies. These two roll angles differ by 11° (ignoring a meaningless 180° rotation.)

Grism data were reduced using the software package Grizli [4]. We followed the steps of the standard Grizli reduction pipeline with a key modification. Because this object is lensed by a galaxy cluster, there are several bright cluster members that contribute significant contamination to the 2D grism spectrum; to best model the contaminating light from these sources, their light profiles in the direct images were first modeled using GALFIT (Peng et al. 2010). Rather than assigning light to these objects using the Source Extractor segmentation maps generated automatically by Grizli, light was assigned to these objects based on their GALFIT models, with the light profiles truncated where the surface brightness fell to less than 0.1% of the central value. These models were subtracted from the direct images, and the preliminary contamination models for these objects were created separately from the contamination models for the rest of the field. After the initial models were made, the two sets of preliminary contamination models were combined before running the standard contamination model refinement steps in the Grizli pipeline. When multiple objects contribute significant contaminating light to the same region in the observed 2D spectrum, this process can better assign that light to the sources responsible for it, and therefore facilitate the production of better contamination models, ultimately yielding cleaner 2D spectral extractions than those produced by the standard Grizli procedure. Figure 3 shows some of the 2D spectra after this process.

[4] https://github.com/gbrammer/grizli

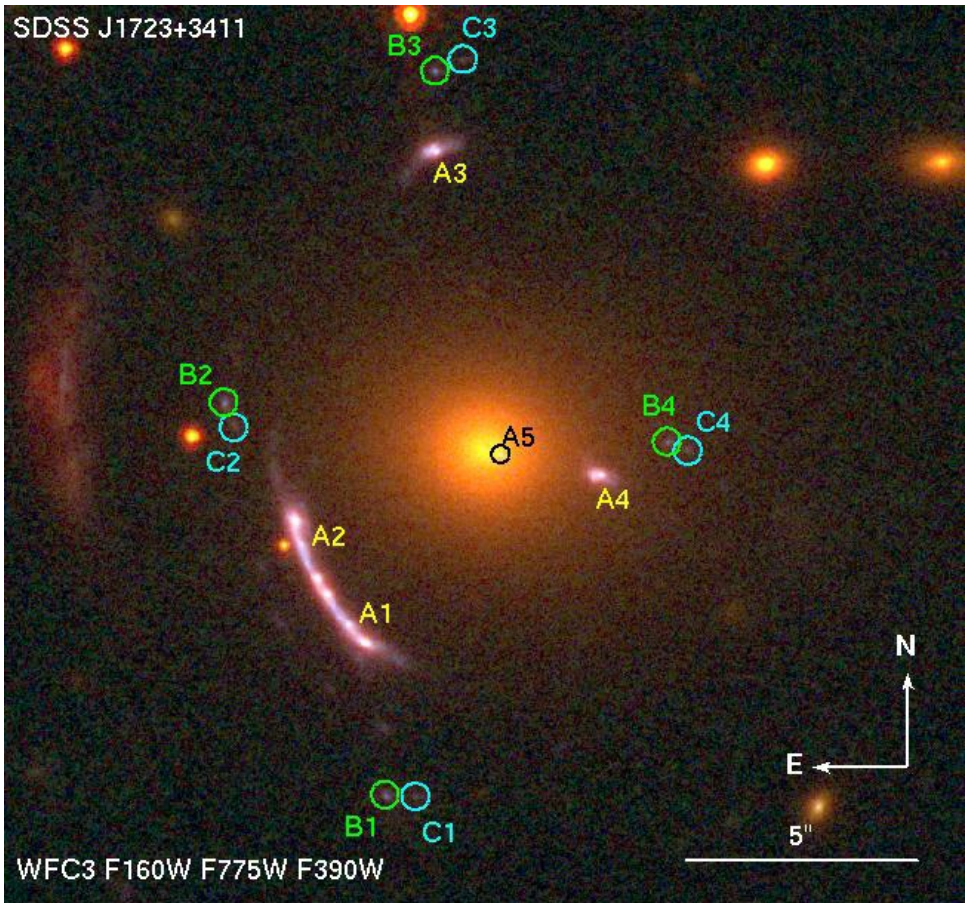

Figure 1. *HST* color composite image of SDSS J1723+3411, with RGB colors set to the F160W, F775W, and F390W filters from the IR and UVIS and channels of the WFC3 instrument. Image families used in the lensing analysis of Sharon et al. (2020) are marked; the bright, multiply-imaged arc "A," encompassing both images A1 and A2, is the subject of this paper.

After extracting the 2D spectra from each grism and each roll angle, 1D spectra were produced by using the flux-weighted center of the arc in each row of the direct images to determine the offsets in the wavelength calibration from row to row in the 2D spectra. We then interpolated each row to subsample the spectrum by a factor of 10, summing the rows in these finer wavelength bins, and then resampling the result to a coarser wavelength grid with bin sizes equal to the original dispersion (i.e., about 46Å per pixel for G141, 23Å for G102). The extracted spectra cover the observed wavelength range of $\sim$ 7800–11900 Å for G102 and 10400–17600 Å for G141, which corresponds to rest-frame wavelengths of 3350–5108 Å and 4460–7555 Å, respectively. To maximize signal-to-noise ratios for line-fitting, we summed together the 1D spectra from each of the two rolls; Figure 4 shows these final spectra. Each 1D spectrum was also fit individually as a consistency check; the offset in the Hα/Hβ ratio from roll to roll is considerably smaller than the measurement uncertainty for a given roll.

2.3.3. *MMT Blue Channel spectra*

We observed SDSS J1723+3411 with the Blue Channel spectrograph (Angel et al. 1979) on the 6.5 m MMT Observatory telescope on UT 2014-05-05 beginning at 09:20 UT. Observing time was granted through the Harvard–Smithsonian Center for Astrophysics. Science exposures of 2400s and 1200s were taken at central wavelengths of 4005Å and 4205Å, respectively, with the spectrograph configured with the 1.25″ wide longslit at a position angle of 29.5° East of North, and the 800 line/mm grating in first order. The source was at low airmass, with $sec(z) < 1.03$. Conditions were clear with sub-arcsecond seeing during the science observations. The science frames were bracketed by HeNeAr arc lamp wavelength calibration frames and quartz lamp flat calibration frames taken at the same position angle. The spectrum was fluxed using observations of standard star Feige 34 that were taken the same night as the science observations, with the same grating settings, and at the same airmass ($sec(z) = 1.02 \pm 0.02$).

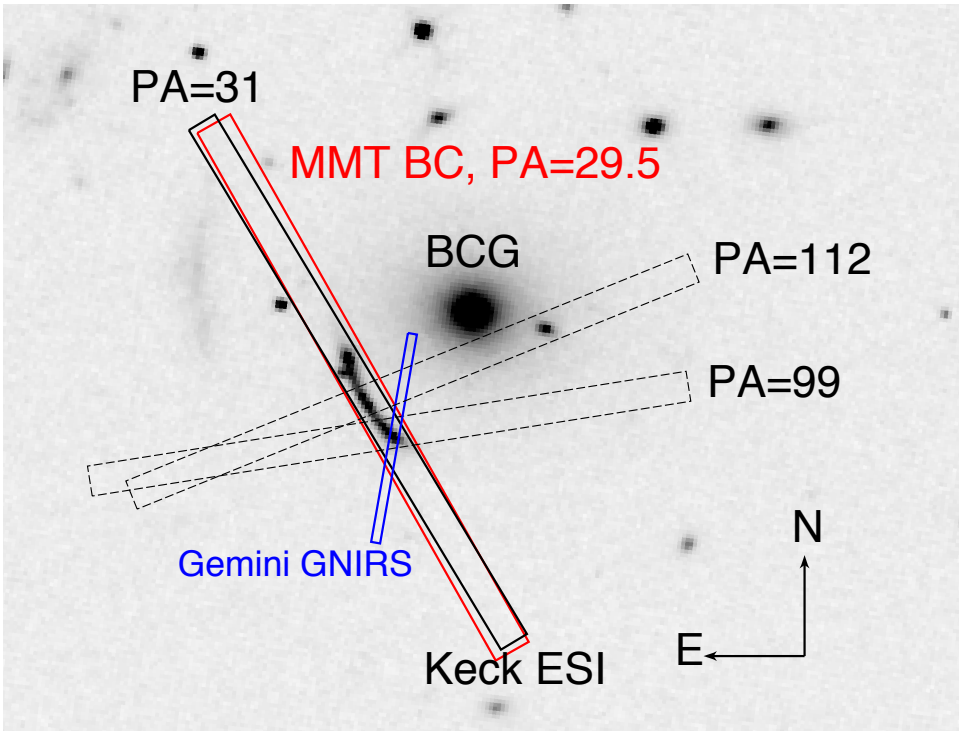

Figure 2. Finderchart to show spectroscopic slit positions for the lensed galaxy SDSS J1723+3411. The background image is *HST* WFC3-IR F105W. The long black rectangles show the Keck ESI pointings (with a 1 by 20″ long slit); the solid shape shows the pointing that captured the giant arc, which is used in this paper. Two additional ESI pointings, which captured portions of the arc, are shown by the dashed rectangle. The long red rectangle shows the MMT Blue Channel slit position (with a 1.25″ longslit). The small blue rectangle shows the Gemini GNIRS pointing, with a 0.3″ by 7″ slit. The brightest cluster galaxy (BCG) is marked.

The Blue Channel spectra were reduced as follows. The spectra were bias-subtracted, flat-field corrected, and wavelength calibrated using standard IRAF routines from the **iraf.noao.imred.ccdred** and **iraf.noao.onedspec** packages. We subtracted the sky on a pixel-by-pixel basis using a two-dimensional model that was generated with custom IDL code that makes use of the XIDL package. The final object spectrum was boxcar extracted from the full object profile of the giant arc, using an aperture that extended approximately 3″ along the spectroscopic slit. The final combined spectrum covers a range in wavelength of ∼3200–5200Å, with a dispersion of 0.75Å per pixel, spectral resolution $R \equiv \delta\lambda/\lambda \simeq 1400$, and a median signal-to-noise of ~ 7 per spectral pixel.

The Blue Channel spectrograph is extremely sensitive in the blue, with sensitivity down to 3000 Å. However, at 3000 Å the Earth's atmospheric transmits only 0.6%, as compared to 17.7% at 3200 Å and 28.7% at 3400 Å (Cox 2000 Table 11.25.) We therefore take $\lambda = 3200$ Å as the blue cutoff. The spectrum effectively thus covers observed wavelengths of 3200–5200 Å, which correspond to rest-frame wavelengths of 1370–2230 Å.

Due to a paucity of emission lines in the calibration lamps, the Blue Channel wavelength solution is uncertain by ∼ 0.4 Å, as measured by comparing the centroids of bright sky lines to the lamp–based wavelength solution.

2.3.4. *Keck ESI spectra*

We obtained spectra of SDSS J1723+3411 using the Echellette Spectrograph and Imager (ESI) on the Keck II telescope (Sheinis et al. 2002), as follows. Observations were made on UT 2016-08-27 and UT 2016-08-28; observing time was granted through Australian National University. The echellette mode and the 1″ slit were used for all observations, which provides a spectral resolution of $R \approx 4000$. Spectra were obtained at several different position angles, as shown in Figure 2. For this paper, we use two integrations, with a total exposure time of 2.055 hr, and a position angle (31° E of N) that put the entire arc in the slit. The airmass was $\sec(z) = 1.04$. The spectrophotometric standard star BD+332642 was observed at the beginning of the night for flux calibration.

We reduced the ESI spectra for each pointing using a combination of IRAF and python routines, as follows. First each raw 2D frame was bias and flat-field corrected.

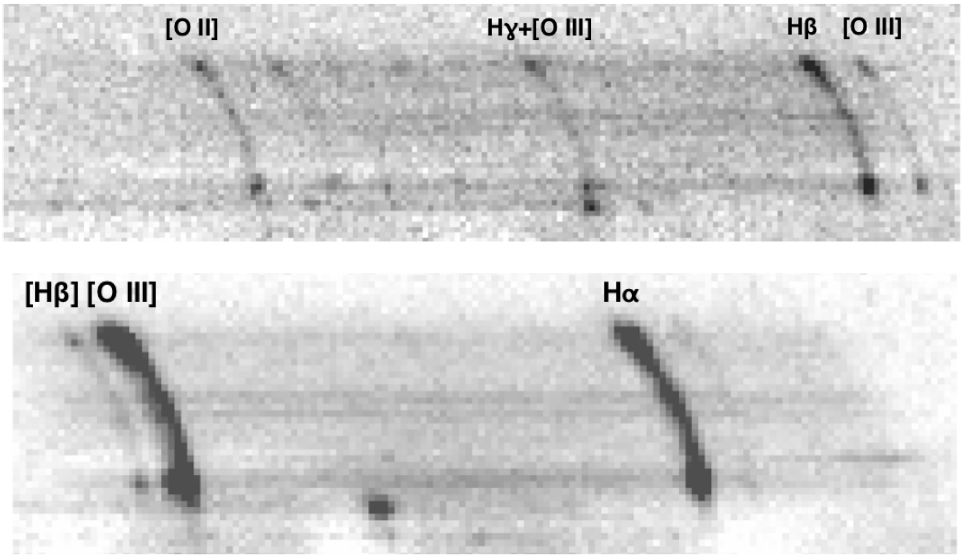

Figure 3. Two-dimensional *HST* WFC3-IR grism spectra of SDSS J1723+3411, at the 139° roll angle, from the G102 grism (top panel) and the G141 grism (bottom panel). Emission from the sky and from contaminating neighbors has been removed. The brightest emission lines are labelled.

Cosmic rays were removed using the IRAF routine *lacos* (van Dokkum 2001). Sky subtraction and spectral extraction were done using the IRAF tool *apall* within the **noao.twodspec.apextract** package, fitting the trace with a second-order Legendre polynomial, and using variance-weighted (also known as optimal) extraction of the target spectra using a 33-pixel wide extraction aperture, and with 17-pixel-wide sky apertures on either side of the target extraction aperture. We performed the wavelength calibration to each extracted echelle order by manually comparing the extracted spectra of CuAr, HgNe and Xe arc lamp exposures to the corresponding template. This led to a wavelength accuracy of at least 0.13%. We used the *standard*, *sensfunc*, and *calibrate* tasks in IRAF's **noao.onedspec** package to flux calibrate each extracted echelle order. The same dispersion solution and flux calibration was applied to spectra from both nights.

We used custom python routines to combine the extracted echelle orders from each observation of the science target within each night into one continuous, calibrated 1D spectrum, using a mean weighted by the inverse variance in regions of order overlap. We then summed the 1D spectra over the multiple nights of observation, with inverse variance weights, applying the barycentric correction in the process. The resulting ESI spectrum covers observed wavelengths of 4000–10000 Å, which corresponds to rest-frame wavelength coverage of 1720–4290 Å.

2.3.5. *Gemini GNIRS spectra*

We obtained spectra of SDSS J1723+3411 with the Gemini Near-Infrared Spectrograph (GNIRS) (Elias et al. 2006a,b) on the Gemini North telescope as part of program GN-2016B-FT-11 (PI Rigby). Observations were obtained on UT 2016-09-07, using the short camera, cross-dispersing prism ("SXD" mode), the 0.3″ slit, and the 111 lines/mm grating with the central wavelength set to 1.529 μm. This setup should provide a spectral resolution of $R = 5900$. The spectra covered observed wavelengths of 1.46–1.60 μm, which correspond to rest-frame wavelengths of 0.627–0.687 μm. Twelve integrations of 270 s duration were obtained; one suffered data quality issues and was discarded. Thus, the effective integration time was 2970 s. As shown in Figure 2, the slit was centered on brightest knot in image A1, and was placed perpendicular to the giant arc. As such, this spectrum covers a very different portion of the giant arc than the Keck/ESI and MMT/Blue channel spectra.

The airmass ranged from $1.06 \leq sec(z) \leq 1.16$. The data were obtained as A−B nods. The grating position was not stable during the observations, which produced noticeable drift from frame to frame in the wavelength solution and in the location of the spectral trace on the detector.

The GNIRS data were reduced to produce a one-dimensional spectrum as follows. We used the Gemini IRAF package, with sky subtraction done by differencing A−B pairs. From each A−B pair, spectra of the A and B images were extracted using a 7 pixel wide boxcar. To mitigate the significant residual skylines due to the grating drift, we extracted a "skyline residual spec-

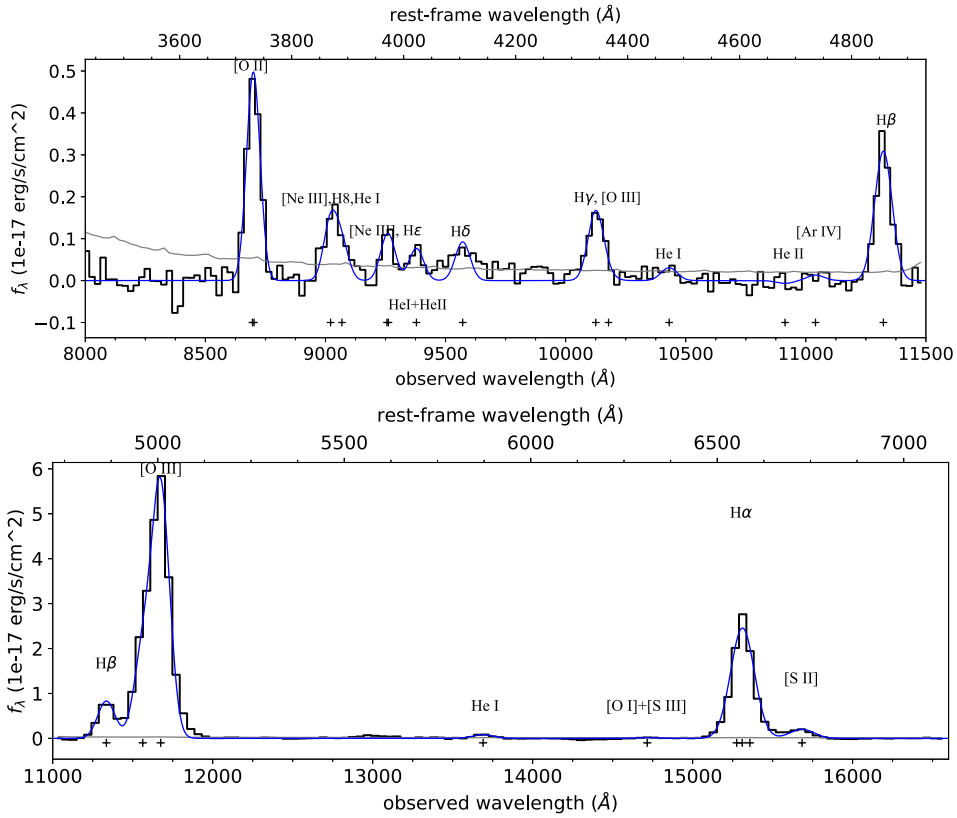

Figure 4. Line-fitting to the summed 1D *HST* WFC3-IR grism spectra, for the G102 grism (top panel) and for the G141 grism (bottom panel.) The black thick line shows the continuum–subtracted spectrum, the thin grey line shows the 1σ uncertainty spectrum, and the blue line shows the best fit. Emission line centroids are marked with crosses.

trum" from each A−B pair, using a 7 pixel wide boxcar located between the A and B positions of the galaxy. We then subtracted the corresponding skyline residual spectrum from each individual extracted spectrum. The resulting 1D spectra were then averaged, and the error in the mean taken as the uncertainty spectrum. The spectra were not absolutely fluxed.

2.4. *Relative flux corrections to the spectra*

The five spectra of SDSS J1723+3411— from the MMT Blue Channel, Keck ESI, *HST* WFC3-IR G102 and G141, and Gemini GNIRS — together provide overlapping, continuous wavelength coverage. The HST WFC3 grism spectra should be the best fluxed, since they do not suffer from seeing, atmospheric transparency variation, or slit losses. We therefore adjust the flux scales of all other spectra to match that of the G141 grism spectrum, as follows:

- We do not apply any relative flux scaling between the G102 and G141 grism spectra, since both are slitless spectra from a space telescope, and therefore do not suffer seeing–dependent slit losses. The flux calibration of the WFC2-IR grisms is excellent (Kuntschner et al. 2011, ST-ECF ISR WFC3-2011-05) and has been temporally stable to better than 1% over four years (Lee, Pirzkal, and Hilbert 2014, STScI ISR WFC3 2014-01).

- We scale the flux of the ESI spectrum to match that of G102, by using the [O II] 3727, 3729 Å doublet. The doublet is spectrally resolved in the ESI spectrum but is blended in G102. Therefore, we scale the flux of the ESI spectrum so that the combined flux in the [O II] doublet matches that in the G102 spectrum. With this scaling, the continua of the ESI and G102 spectra overlap at 8470 Å, close to the observed position of the [O II] 3727, 3729 Å.

- We scale the flux of the Blue Channel spectrum to that of the ESI spectrum, using the [C III] 1907, C III] 1909 Å doublet. The doublet is spectrally well-resolved in the ESI spectrum, but is blended in the lower–resolution Blue Channel spectrum. Therefore, we scale the flux of the Blue Channel spectrum so that the combined flux in the C III doublet matches that of the ESI spectrum. With this scaling applied, the median f_λ in the line–free

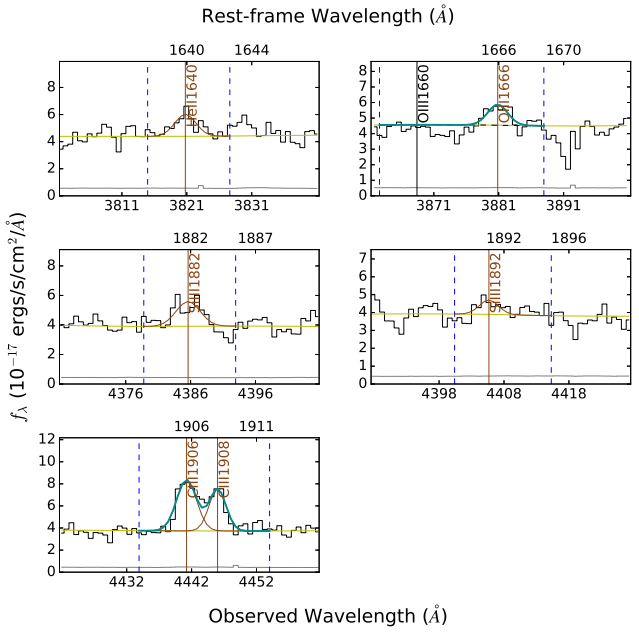

Figure 5. Detected emission lines and Gaussian line fits in the MMT Blue Channel spectrum of SDSS J1723+3411. Black steps show the spectrum, brown vertical lines show the best–fit central wavelength of detected ($> 3\sigma$) lines, brown Gaussians show the individual components of the fit, and thick green lines show the sum of multiple fitting components. The 1σ uncertainty spectrum is shown in grey. Black vertical lines denote non-detection ($< 3\sigma$). The fitting routine works on a portion of the spectrum as shown bounded by blue dashed lines.

region 4200–4300 Å for Blue Channel and for ESI agree to within 2%.

- The Gemini GNIRS spectra are not absolutely fluxed, so we do not attempt any relative flux calibration. None is needed, since the GNIRS spectrum is only used to obtain the flux ratio of the [N II] lines to nearby Hα.

2.5. *Measuring emission lines*

We measure emission line fluxes as follows; measurements are tabulated in Table 1.

2.5.1. *Fitting lines in the ESI and MMT spectra*

To fit an empirical continuum to each of of the MMT Blue Channel and Keck ESI spectra, we mask the expected positions of ISM absorption lines, nebular emission lines, and stellar wind lines, and then boxcar smooth the spectrum.

For the continuum-subtracted Keck and MMT spectra, we simultaneously fit all emission lines using the methodology of A19. Examples are shown in Figure 5 and Figure 6. Briefly, neighboring emission lines (defined as within ±5 spectral resolution elements) are fit with Gaussians simultaneously, with the line centers allowed to move by 3σ from the expected position given the systemic redshift, which we assume to be the redshift of Hα measured in GNIRS/Gemini (see §3.3.) Line widths are bounded between a spectral resolution element and 300 km s^{-1}. Flux and equivalent widths are measured from this fitting process. We also report the significance of the feature following the method of Schneider et al. (1993), which indicates how significant the line is given the noise in the spectrum, without prior knowledge of the redshift. We consider a line to be detected if has a Schneider et al. significance greater than 3, and if its measured flux is greater than the flux uncertainty. For undetected features, we quote the Schneider et al. 3σ limits on flux and equivalent width.

2.5.2. *Fitting lines in the WFC3-IR grism spectra*

The grism spectra require a different approach to measuring emission line fluxes, since the very low spectral resolution means that linewidths are set entirely by the disperser and by the morphology of the target relative to the dispersion direction, and since the wavelength calibration accuracy is much worse than from an echelle spectrograph. For each grism spectrum, we fit an empirical continuum using the XIDL package x_continuum, in which the portions of the spectrum that are free of emission lines were fit with a ninth-order Legendre polynomial. The emission lines in each continuum-subtracted grism spectrum were then fit as follows, with separate fits to the G102 and G141 spectra. We use the python package LMFIT, which implements non-linear least-square minimization and curve-fitting (Newville et al. 2016). The width of each emission line was not free to vary, but instead set by the following assumptions: that the instrumental line spread function is Gaussian, that the lines are spectrally unresolved, that the intrinsic spectral resolution R_i of each grism (as would be appropriate for a point source) is $R_i = 210$ for G102 and $R_i = 130$ for G141 (Gennaro 2018), and that the observed spectral resolution can be approximated as $R_o = R_i/m$, where m is a morphological broadening factor for that spectrum, which is solved for in the fitting process. This morphological broadening occurs because the grism spectra are slitless; it approaches unity for a thin source aligned perpendicular to the dispersion direction, and is high when the source elongation is aligned with the dispersion direction.

We fit 14 emission lines to the G102 spectrum, and 9 emission lines to the G141 spectrum, as shown in Figure 4, with results listed in Table 1. Since the [S II] 6718, 6732 Å doublet is unresolved at the grism resolution, and since the ratio is not constrained by other

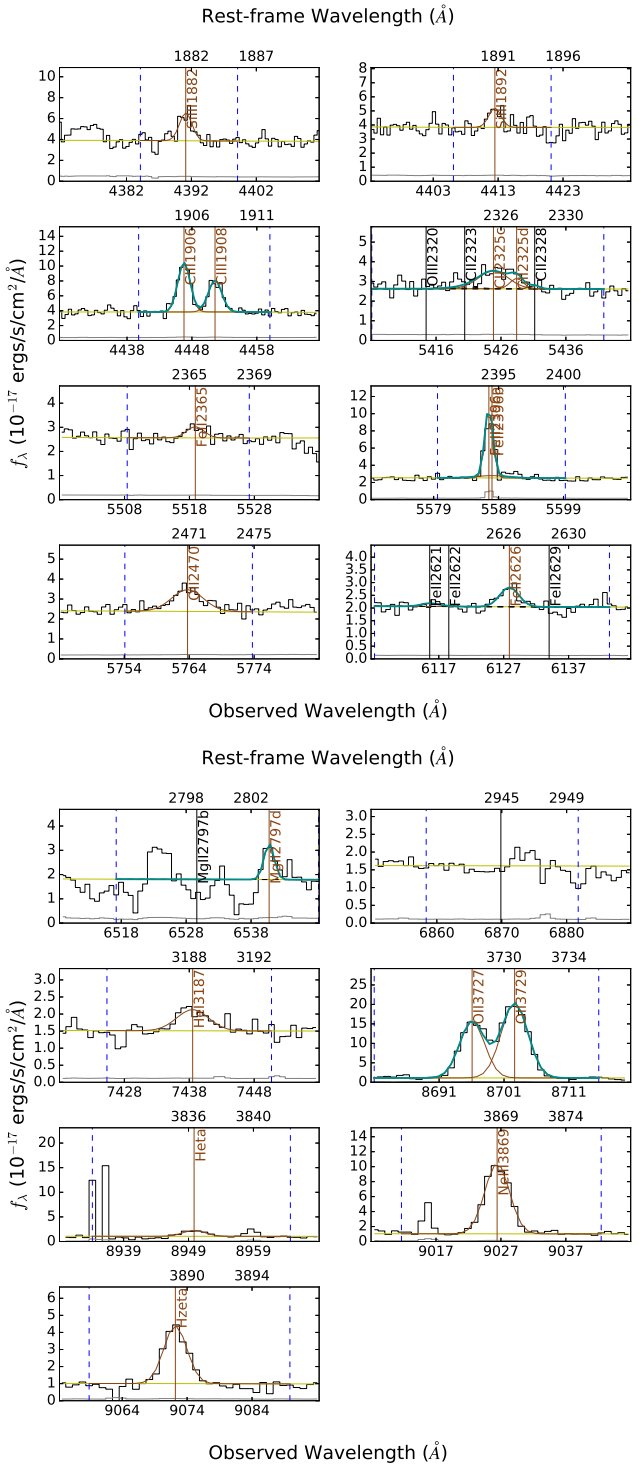

Figure 6. Detected emission lines and Gaussian line fits in the Keck ESI spectrum of SDSS J1723+3411. Labels and color codes are as in Figure 5.

spectra, we fit it with a single Gaussian. We do the same for the blend of H8 and He I near 3890 Å, and the blend of [O I] and [S III] near 6310 Å.

We fix the following doublet ratios to their theoretical values from Storey & Zeippen (2000): [Ne III] 3870.16, 3968.91 Å; [N II] 6549.85, 6585.28 Å; and [O III] 4960.295, 5008.240 Å. At the low spectral resolution of the WFC3-IR grisms, the [N II] doublet is blended with Hα, and the [O II] 3727, 3729 Å doublet is not resolved. Therefore, we fix the [O II] doublet ratio to that measured from the ESI spectrum (see §2.5.1), and fix the ratio of [N II] 6585 / Hα to that measured from the Gemini GNIRS spectrum (see §2.5.3).

The dispersion solutions for the WFC3-IR grisms have an internal accuracy 6Å for G102 and 9 Å for G141 (Gennaro 2018, see §9.3.8); these are significant fractions of a pixel. To compensate, we fit the spectra with a two-step process. In the first step, we fit each spectrum by solving for a common redshift, a morphological broadening factor, and the flux of each unconstrained emission line. In the second step, we fix the redshift as the result from step 1, and re-fit the spectra, again solving for the morphological broadening factor and the line fluxes, but this time allowing the wavelengths of groups of neighboring lines to shift by a common offset. The resulting wavelength offsets are within the range expected given the internal accuracy of the wavelength solution.

The grism spectra should have excellent fluxing accuracy, since they are slitless and obtained from space. Small changes in the fluxing can occur due to roll-dependent differences in the contamination model and the extraction region. For G102, the fluxes of the three brightest lines scale by 2% and 8% for the two individual rolls compared to the spectrum extracted from both rolls combined. For G141, the fluxes of the three brightest lines scale by -6% and $+4$% for the two individual rolls compared to the spectrum extracted from both rolls combined. For the rest of the analysis, we use the fluxes extracted from the combined spectra from both rolls.

In order to fit the multiple line blends in the grism spectra, it was necessary to assume a line-spread function. We now examine the impact of that assumption, using a relatively isolated line. In G102, the brightest isolated line is Hβ: direct summation of the continuum–subtracted spectrum returns 8% higher line flux than from line fitting. Direct summation produces fluxes that are 6% higher for [O II] 3727, 3729 Å (again in the G102 grism), and 3% lower for the [N II]+Hα blend (in the G141 grism). Thus, there appears to be a several percent uncertainty in measuring a line flux, which may be attributed to the detailed shape of the line-spread profile.

2.5.3. *Fitting lines in the Gemini GNIRS spectrum*

We fit the 1D GNIRS spectrum with Gaussians using the IDL Levenberg-Marquardt least-squares fitting code MPFIT (Markwardt 2009), following the method described in Wuyts et al. (2014). The continuum was assumed to be flat over the wavelength region of interest, and the continuum level was allowed to vary. The flux ratio of the [N II] doublet was locked at the value from Storey & Zeippen (2000). The central wavelengths of each line was set using the rest wavelength from NIST and the measured Hα redshift in the 1D spectrum, and allowed to vary by $\pm 3\times$ the 1σ uncertainty in the central wavelength of Hα. The uncertainty spectrum was used as weights in the fitting, which prevented adjacent residual skylines from biasing the fit. The redder transition of [N II] is adjacent to a skyline, but is clearly detected. The linewidths were tied together, and the width of the linespread function was varied, minimizing chi-squared.

The [S II] doublet was not detected in the GNIRS spectrum, and so was not fit.

3. RESULTS

3.1. *A new spectral template for emission–line galaxies*

In Figure 7, we present a contiguous spectral template of the bright gravitationally–lensed galaxy SDSS J1723+3411, completely covering the rest-frame wavelength range 1375 to 7230 Å, in which 42 individual emission lines are detected. We electronically publish this template and provide electronic versions of the reduced spectra from the four individual spectrographs. We expect these spectra should be helpful to investigators preparing observing programs with the *James Webb Space Telescope*, as well as other applications.

3.2. *Luminosity and stellar mass*

From the *HST* imagery, Florian et al. (submitted) compute observed AB magnitudes for the giant arc of 20.6, 20.5, 19.9, 20.2, 20.2, and 20.1 in the F390W, F775W, F105W, F110W, F140W, and F160W filters, respectively (see their Table 4.) Given those magnitudes and the magnification reported by Florian et al., we calculate that the absolute magnitude at rest-frame 1700 Å is -19.95. This is very similar to the $M^*_{1700} = -19.8^{+0.32}_{-0.26}$ reported at $z = 1.7$ by Sawicki & Thompson (2006). As such, while SDSS J1723+3411 appears to be one of the brightest lensed galaxies known, its intrinsic UV luminosity is typical for star-forming galaxies at its redshift.

From Hα fluxes measured in the *HST* grism spectra, and the conversion of Kennicutt (1998), Florian et al. estimate a total star formation rate for SDSS J1723+3411 of 7.9 ± 0.4 M$_\odot$ yr^{-1}, from the northern complete image (image 3.) Based on photometry from *HST* and *Spitzer*, the lens model of Sharon et al. (2020), and the Prospector MCMC-based stellar population synthesis code (Johnson & Leja 2017), Florian et al. (submitted, see their Appendix) estimate a stellar mass for SDSS J1723+3411 of $5.95^{+2.2}_{-1.86} \times 10^8$ M$_\odot$. Thus, SDSS J1723+3411 lies a factor of 12 above the star formation rate–stellar mass relation at $1.0 < z < 1.5$ (Whitaker et al. 2014). Comparisons to similar compilations by Tomczak et al. (2016) and Santini et al. (2017) yield a similar result: SDSS J1723+3411 lies about a factor of 10 above the star formation rate–stellar mass relation for its redshift. It is thus a "starburst" galaxy experiencing significantly more star formation than is typical for galaxies of its stellar mass at $z = 1.3$.

3.3. *Redshift of Hα*

To mitigate the problem that the grating drifted during the GNIRS observations, we measure the redshift of $H\alpha$ from a subset of the two-dimensional GNIRS data, as follows. For each integration, we produce an A−B (or B−A) difference image. For the 6 cleanest difference images (of 11), we measured the position of Hα relative to the positions of two bright skylines (at known vacuum wavelengths of $\lambda_{vac} = 15241.0$ and 15332.4 Å), and assumed a linear dispersion across this small wavelength range. We test the accuracy and precision of this procedure by measuring the wavelength of a third, fainter skyline, at $\lambda_{vac} = 15287.8$ Å; we recover its wavelength to an accuracy of 0.1 Å.

We measure the wavelength of Hα, and apply the barycentric correction, resulting in a $\lambda_{vac}(H\alpha) = 15290.8 \pm 0.6$ Å (quoting the median of the measurements and the standard deviation.) We thus measure the redshift as $z(H\alpha) = 1.3293 \pm 0.0002$. This is the best determination of the systemic (nebular) redshift for this galaxy.

This measured redshift is fully consistent with that measured by Kubo et al. (2010), of $z = 1.3294 \pm 0.0002$, measured from the [C III] 1907, C III] 1909 Å and [O II] 3727, 3729 Å. This measured redshift is also similar to the redshift of $z = 1.328$ (no uncertainty quoted) measured by Stark et al. (2013) from the [C III] 1907, C III] 1909 Å doublet and ISM absorption lines.

3.4. *Reddening*

We use the Balmer line ratios to determine the amount of reddening of the nebular lines. Table 2 lists the observed line ratios and the inferred $E(B-V)$ reddening for the spectra from each of the two roll angles, as well as from the roll–combined spectra. By experimental design, Hβ falls in the few hundred Angstrom region where

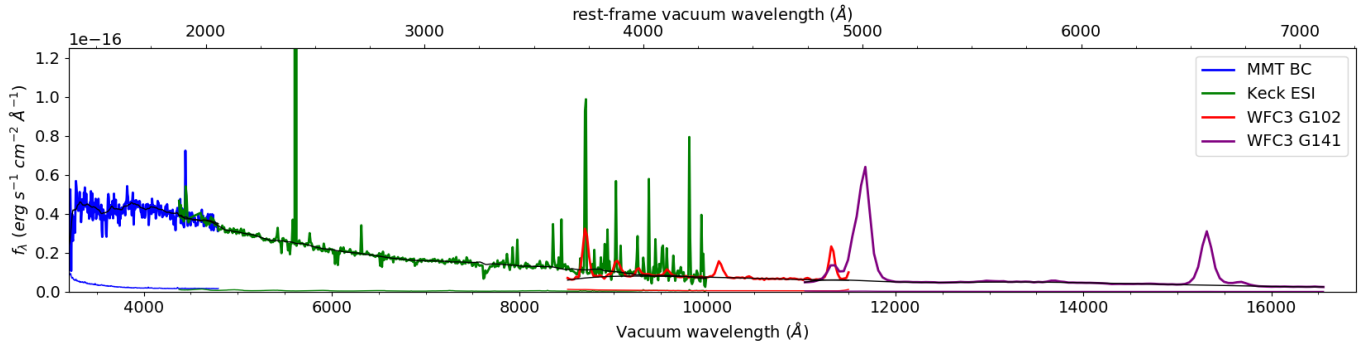

Figure 7. Four of the five spectra for SDSS J1723+3411. From left to right, the spectra shown are from the MMT Blue Channel, Keck ESI, HST WFC3-IR G102, and HST WFC3-IR G141. The MMT and Keck spectra have been median smoothed with a boxcar for readability. The flux scaling of the MMT and Keck spectra have been adjusted as follows: The Keck ESI spectrum has been scaled to match the flux in the [O II] 3727, 3729 Å emission lines in the G102 spectrum, and the MMT Blue Channel spectrum has been scaled to match the flux in the [C III] 1907, C III] 1909 Å emission lines in the ESI spectrum. For readability, most of the overlap between the spectra is not shown. The 1σ uncertainty spectra are shown with the same color-coding as the science spectra, and the fitted continua are shown as thin black lines.

the G102 and G141 grisms overlap in wavelength at high sensitivity. We believe the flux is measured more accurately and precisely by the G102 grism, for several reasons. First, the higher spectral resolution of G102 more cleanly separates the Hβ line from the [O III] doublet. Second, Hβ in SDSS J1723+3411 falls near the edge of the G141 wavelength coverage, where the flux calibration is more uncertain. Third, in the 139° roll, the G141 grism spectrum suffers from some contamination by the counter-image "A4" that affects the measurement of Hβ . The flux of Hβ measured in each grism agrees to within 9% (139° roll) and 19% (308° roll). Table 2 shows that when the Hα/Hβ ratio is measured using G102 for Hβ and G141 for Hα, the result is not dependent on roll angle, and the uncertainties are low: the value measured from the roll-combined spectrum is Hα/Hβ= 2.96 ± 0.1, which is slightly higher than the values measured from each roll: 2.86 ± 0.1 (308° roll) and 2.86 ± 0.1 (139° roll).

By contrast, when both Hα and Hβ are measured from G141, the measured values are higher (3.1 to 3.7), with larger uncertainties (± 0.2), and with a a roll dependence that is larger than the uncertainties.

Thus, the more reliably measured Balmer ratio is Hα/Hβ= 2.96 ± 0.1, with Hβ measured from G102 and Hα from G141, from the roll-combined spectra. This is quite close to the intrinsic value, and indicates that the reddening is very low: $E(B-V) = 0.028 \pm 0.04$ mag.

Higher-order Balmer line ratios are also measured: Hβ/Hγ and Hβ/Hδ. The fluxes of the higher-order Balmer line fluxes are measured less precisely than Hβ, due to their relative faintness and the blending of Hγ with [O III] 4363 Å in the G102 grism. Nevertheless, the reddening inferred from the higher-order Balmer line ratios is consistent, with the uncertainties, with the more precise measurement from Hα/Hβ.

3.5. *[N II] / Hα ratio*

Figure 8 shows the 2D GNIRS spectra, the extracted 1D GNIRS spectrum, and the best fit to Hα and [N II]. From fitting the 1D Gemini GNIRS spectrum, we measure the [N II] 6586 / Hα flux ratio as 0.062 ± 0.01. This corresponds to an oxygen abundance of $12+\log(O/H) = 8.21 \pm 0.04$ (31% of solar) using the linear calibration of Pettini & Pagel (2004), and 8.19 ± 0.03 (29.5% of solar) using their third-order calibration. The calibration of Kewley et al. (2019b) yields a higher metallicity, $12 + \log(O/H) = 8.62 \pm 0.01$ assuming a pressure of $\log(P/k) = 6$. As noted above, the GNIRS spectrum covered only one sub-region of giant arc, and is therefore not strictly comparable to the measurements from Keck/ESI, MMT/Blue Channel, and *HST*/ WFC3-IR, which covered the entire giant arc.

3.6. *Comparison of rest-frame optical diagnostic diagrams and equivalent widths*

Line ratio versus line ratio diagrams, including [O III]/Hβ versus [N II]/Hα or versus [S II]/Hα (the so-called BPT diagrams, Baldwin et al. 1981), and O32 versus R23 or versus O3N2, are a standard tool to classify the spectra of galaxies. Multiplexed spectroscopic surveys of field galaxies at $z \sim 2$ have revealed marked evolution in these diagrams since $z = 0$ and $z \sim 2$ (Kewley et al. 2013b; Steidel et al. 2014; Shapley et al. 2015). It is therefore instructive to locate SDSS J1723+3411 on these diagrams. Figure 9 of Sanders et al. (2016) plots O32 versus R23 for the SDSS sample at $z \sim 0$ and the MOSDEF sample at $z \sim 2$. Compared to both samples,

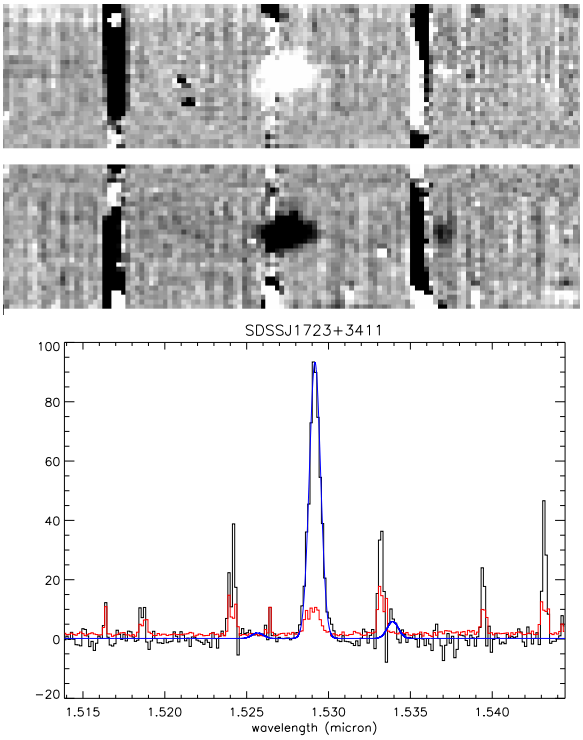

Figure 8. The Gemini GNIRS spectrum of SDSS J1723+3411. Left panel: The Hα region of the two-dimensional spectrum, with the sum of the A nods at top, and the sum of the B nods at bottom. Wavelength increases to the right; Hα is centered. This is a zoom in covering wavelengths of approximately 1.522–1.538 μm. The blue wing of H alpha is mildly contaminated by a sky line; [NII 6586] falls just redward of a skyline, and is confidently detected in both nods. Right panel: The resulting extracted 1D spectrum of Hα and [N II] in SDSS J1723+3411. Plotted is the average spectrum out of 11 integrations (black steps), the error in that mean (red steps), and the best-fitting Gaussians from MPFIT (blue steps).

SDSS J1723+3411 sits at the top of both the O32–R23 relation and the O32–O3N2 relation; thus its emission lines ratios are extreme compared to both SDSS and to MOSDEF. Green pea galaxies also inhabit the upper tip of the O32–R23 relation (Jiang et al. 2019). Figure 11 of Sanders et al. (2016) plots the [N II] and [S II] BPT diagrams for SDSS and for MOSDEF; SDSS J1723+3411 sits on the upper left wing of both diagrams, with emission lines that are extreme even compared to the typical $z \sim 2$ galaxies of MOSDEF. Kewley et al. (2013a) argue that that regime of the BPT diagrams should be populated given some combination of higher ionization parameters, harder ionizing spectra, and higher electron density compared to SDSS at $z \sim 0$.

Also striking are the high equivalent widths of the rest-frame optical emission lines in SDSS J1723+3411. To be quantitative, SDSS J1723+3411 has a combined rest-frame equivalent width of Hβ, [O III] 4959, and [O III] 5007 Å of 1029±7Å. This is even higher than the median equivalent widths of 670^{+260}_{-170} Å, 649^{+49}_{-52} Å, and 692^{+102}_{-103} Å inferred through fitting photometry to color-selected $z \sim 7$–8 galaxies of, respectively, Labbé et al. (2013); de Barros et al. (2019), and Endsley et al. (2020). This is also the regime of high equivalent width that is characteristic of the so-called "green pea" galaxies at $z \sim 0.1$–0.4, which are selected to have [O III] 5007 Å equivalent widths exceeding 300 Å (Cardamone et al. 2009; Jiang 2018).

3.7. *Comparison of UV emission-line equivalent widths*

Recent surveys have captured the rest-frame UV emission lines in a number of galaxies in the local universe, and at moderate to high redshift. The total [C III] rest-frame equivalent width of SDSS J1723+3411, −3.5±0.3 Å from the MMT/BC spectrum and −3.0±0.1 from the Keck/ESI spectrum is within the large range observed for UV-bright $z \sim 0$ galaxies (Rigby et al. 2015), it matches the median equivalent width of −3.3 Å for a sample of $z \sim 0.2$ Green Pea galaxies (Ravindranath et al. 2020), and is not quite as strong as the median equivalent width of −4.8 Å for a sample of extreme emission line galaxies (Senchyna et al. 2020).

Comparing to more distant samples, the [C III] equivalent width is larger than average but not unusual for lensed $z > 1$ galaxies (Rigby et al. 2015). Comparing the [C III], He II 1640 Å, O III] 1666 Å, and [Si III] 1883 Å rest-frame equivalent widths to stacks of $z \sim 3$ Lyman alpha emitters in Feltre et al. (2020), the equivalent widths for SDSS J1723+3411 are entirely in line with the Feltre sub-samples that are UV-bright, are in the same stellar mass bin, and the same bin of star formation rate. In addition, a sample of extreme [O III] 5007 Å emitters at $1.3 < z < 3.7$ has a median rest-frame C III] equivalent width of −5.7, which is about twice as high as for SDSS J1723+3411 (from Table 5 of Tang et al. 2020). [O III] 1660, 1666 Å was not detected in enough of their spectra to compare the equivalent width to SDSS J1723+3411.

Thus, the equivalent widths of the rest-frame UV lines in SDSS J1723+3411 are entirely within the range observed for extreme galaxies at $z \sim 0$, and at $z \sim 1$–3.

3.8. *Strong emission-line diagnostics*

A19 intercompared the various strong emission-line diagnostics of nebular physical conditions within a star-forming region of the $z = 1.70$ lensed galaxy RCSGA 032727−132609. Their Table 4 describes the line ratio(s) used for each diagnostic. Here, we calculate the same diagnostics for SDSS J1723+3411, and analyze the

results and the degree to which the diagnostics agree. Figure 9 compares multiple strong emission line diagnostics for the physical parameters of the ionized gas in SDSS J1723+3411. Table 4 tabulates the inferred physical parameters. We use diagnostics from Kewley et al. (2019a), Kewley et al. (2019b), and Byler et al. (2020); we do not use historical diagnostics since they used older atomic data. We now consider each physical parameter in turn, starting at the top left of Figure 9. For each parameter, we explain which diagnostics we consider most trustworthy and why; these are highlighted in Figure 9. We then compare to the other available diagnostics, to see which diagnostics are reliable, and which are not.

Electron temperature: For SDSS J1723+3411, as was true for RCS-GA 032727−132609, the best constraint on electron temperature T_e comes from the detection of the UV auroral lines [O III] 1660, 1666 Å, in combination with the rest-frame optical [O III] 5007 Å line; this diagnostic is marked "O3b" in Figure 9. In the MMT spectrum, only the 1666 Å line is detected; the 1660 Å line flux is inferred since the line ratio is set by atomic physics. The inferred T_e is 10700 ± 500 K. The main drawback of this diagnostic is its susceptibility to reddening given the large wavelength span between 1660 Å and 5007 Å; for SDSS J1723+3411 the resulting constraint is particularly tight because the reddening is very low.

By contrast, the diagnostics which rely on the [O III] 4363 Å auroral line (O3a_I06 and O3a_N20 in Figure 9) provide poorer constraints for both SDSS J1723+3411 and RCS-GA 032727−132609. For SDSS J1723+3411 the constraint is particularly poor because at the low spectral resolution of the G102 grism, [O III] 4363 Å is badly blended with Hγ. This faint auroral line will be much easier to capture with *JWST*.

Pressure: For SDSS J1723+3411, the best constraints on nebular pressure come from the [O II] 3727, 3729 Å ratio; the calibrations in Kewley et al. (2019a) yield an ISM pressure of $\log(P/k) = 6.02^{+0.15}_{-0.34}$, which is independent of ionization parameter.

By contrast, the ISM pressure that one would infer from the UV [C III] 1907, C III] 1909 Å lines is higher by 1.5 dex, at $\log(P/k) = 7.6^{+0.37}_{-0.52}$. This effect is predicted to occur as a result of the UV lines arising in more highly ionized region of the nebula, closer to the ionizing sources, than where the [O II] is emitted (Kewley et al. 2019a). A similar (1 dex) offset was seen in RCS-GA 032727−132609 by A19.

Metallicity: The [N II] λ6584/[O II] λ3727 line ratio is the most sensitive to metallicity and least sensitive to the effects of ionization parameter and nebular pressure. It is particularly well-suited to SDSS J1723+3411 since the reddening is low. The dereddened log [NII]/[OII] ratio of -0.87 ± 0.04 yields a metallicity of $\log(O/H)+12 = 8.62 \pm 0.03$, which is 79% of solar. This estimate is independent of ionization parameter unless the ionization parameter is small (i.e. $\log(U) \lesssim -3.0$), and is also independent of ISM pressure. This metallicity estimate agrees with the [N II]/Hα ("N2") metallicity estimate of $\log(O/H) + 12 = 8.62 \pm 0.01$. The optical R23[5] ratio is 0.93, which is above the theoretical models used to calibrate R23. Large R23 values can occur when the metallicity is around the R23 local maximum, which occurs around $\log(O/H) + 12 = 8.4 \pm 0.1$ (48% of solar). Patricio et al. (2018) noted that 10 of the 16 lensed $z \sim 2$ galaxies in their sample had R23 values exceeding the theoretical maximum.

Disappointingly, we find that the metallicity diagnostics that use only rest-frame UV emission lines provide very different constraints than the optical metallicity diagnostics. Neither "N2O2b" ≡ [N II] 2140 / [O II] 2470 nor "N3O3" ≡ [N III] 1750 / [O III] 1660,6 are unable to constrain the metallicity, even though the rest-frame UV spectrum is of high quality. The UV–only "Si3-O3C3' and "He2-O3C3"diagnostics of Byler et al. (2020)[6] indicate metallicities that are 0.5 and 0.8 dex lower, respectively, than what the optical diagnostics yield. This discrepancy is much larger than the uncertainties.

The T_e–based diagnostic of [O III] 1660,6 / [O III] 5007 is able to constrain the metallicity, giving a value 0.3 dex below that from the optical metallicity diagnostics of [N II]/[O II] and [N II]/Hα. This discrepancy between the strong line diagnostics and the T_e method is well known (Stasińska 2005; López-Sánchez et al. 2012).

Ionization parameter: The most reliable ionization parameter diagnostic in this case is the optical "O32a" ratio,[7] which is dependent on the ISM pressure and on the metallicity. Using a pressure of $\log(P/k) = 6$, we derive an ionization parameter of $\log(U) = -2.1 \pm 0.03$, which is $\log(q(\mathrm{cm/s})) = 8.38 \pm 0.03$. This value is broadly consistent with the ionization parameter that we derive from the UV C32b ratio of $\log(U) \geq -2.0$, which is $\log(q(\mathrm{cm/s})) \geq 8.5$.

The optical O32 diagnostic has an analogue in the UV, which uses the [O III] 1660,1666 / [O II] 2470 ratio ("O32b" in Figure 9.) Kewley et al. (2019b) found that this diagnostic depends strongly on metallicity, and should not be used at large pressures and low metallic-

[5] R23 ≡ ([O III] 4959, 5007 Å + [O II] 3727, 3729 Å) / Hβ

[6] We use the fourth-order polynomial fits published in their §5.4.

[7] O32 ≡ [O III] 5007 Å / [O II] 3727, 3729 Å

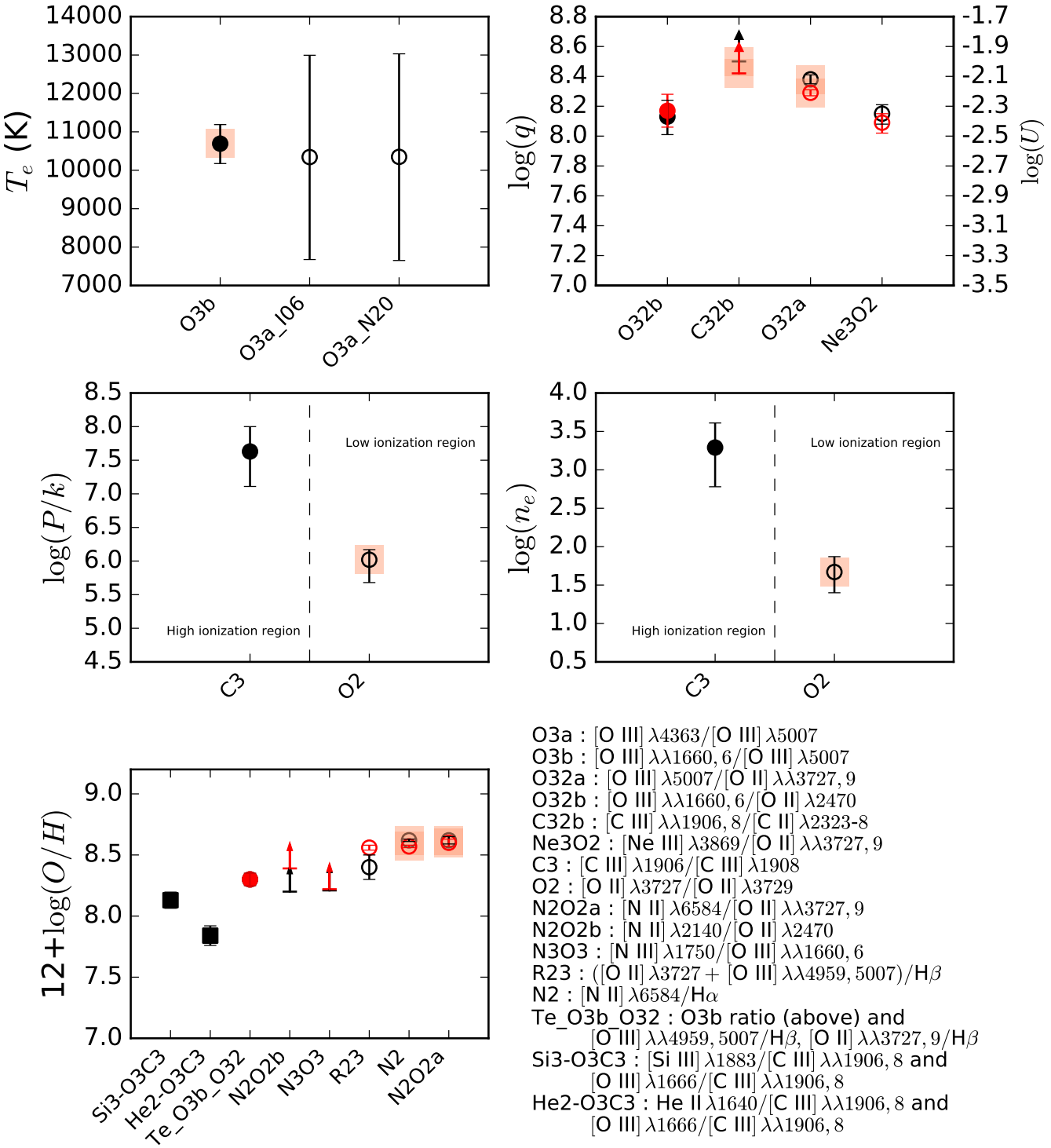

Figure 9. Comparison of strong emission line diagnostics for physical parameters of the ionized gas in SDSS J1723+3411. In each panel, a point denotes the median of the probability density function of the measured physical quantity generated by performing every diagnostic 10^4 times; error bars show the 16^{th} and 84^{th} percentile values. Rest-frame UV diagnostics are denoted by filled symbols, and optical diagnostics by open symbols. The diagnostics we consider most reliable are highlighted in peach. In the bottom left and top right panels, the color coding indicates the pressure assumed for the diagnostic: black symbols assume $\log(P/k) = 6$ K/cm^{-3} (as inferred from the optical), and red symbols assume $\log(P/k) = 7$ K/cm^{-3} (as inferred from the UV). In each panel, the x-axis lists a short-hand name for each spectral diagnostic; the key to the labels is given at bottom right. The spectral diagnostics are as defined in Kewley et al. (2019a) and Kewley et al. (2019b), and are also listed in Table 3. The "_I06" and "_N20" suffixes on the O3a T_e diagnostics refer to the calibrations of that diagnostic from Izotov et al. (2006) and Nicholls et al. (2020), respectively. The y axes of the top right panel show the ionization parameter in both its dimensionless and dimensional forms, U and q, where $U = q/c$.

ities. As discussed above, the pressure in the [O III] zone, as inferred from the UV [C III] 1907, C III] 1909 Å lines, is indeed extremely high. As such, for SDSS J1723+3411, the UV O32b diagnostic is less sensitive to ionization parameter than to metallicity and pressure, and should not be used. Indeed, we find that the ionization parameter one would infer from the UV O32 diagnostic ("O32b") is 0.25 dex lower than from optical O32 ratio ("O32a"). A similar (0.2 dex) offset was seen by A19, with the opposite sign.

Density: If one assumes a constant electron temperature, then the electron density calculated using the [O II] 3727, 3729 Å doublet ratio is $n_e \sim 40 \pm 10$ cm^{-3}, where the errors are due to the residual metallicity dependence of the [O II] electron density relation (see Kewley et al. 2019a). If the electron temperature is not constant, the ISM pressure is a more realistic quantity to measure using the [O II] doublet; pressure and density are simply related as $n_e = P/T_e k$. For the same reason as the pressure diagnostics, the UV [C III] 1907, C III] 1909 Å diagnostic yields a much higher density than does the optical [O II]/[O II] ratio.

4. DISCUSSION AND CONCLUSIONS

This paper presents overlapping, complete spectra from Keck, MMT, Gemini, and *HST* that fully cover the wavelength range $1375 < \lambda_{rest} < 7230$ Å for the extremely bright, gravitationally–lensed galaxy SDSS J1723+3411 at redshift $z = 1.3293$. The spectra have been relatively flux calibrated using bright emission lines, removing the possible systematic effect of relative flux errors that appear in previous work. As such, the spectra published electronically in this paper represent one of the highest-quality empirical templates of star-forming galaxies available at any redshift. We expect that this template will prove useful to the community in planning observations with telescopes including *JWST*.

SDSS J1723+3411 has an intrinsic UV luminosity that is very close to what is characteristic for star-forming galaxies at its redshift. Its star formation rate is a factor of 12 above the star formation rate–stellar mass relation at its redshift, indicating that it is a "starburst" galaxy experiencing much more rapid star formation than is typical for galaxies of its stellar mass at redshift $z = 1.3$. Though SDSS J1723+3411 has a modest redshift of $z = 1.3293$, its properties are consistent with the most extreme galaxies known. Its emission line ratios place it in the extreme tip of the O32–R23 and O32–O3N2 diagnostic diagrams and in the upper left wing of the [N II] and [S II] BPT diagrams, and has the extremely high equivalent widths of Hβ and [O III] 4959, 5007 Å that are characteristic of extreme emission line galaxies like the "green peas" at $z \sim 0.3$ and star-forming galaxies at $z \sim$ 7–8x. Its rest-frame UV emission line equivalent widths are within the range observed for extreme galaxies in the nearby and distant universe. As such, SDSS J1723+3411 should serve as an appropriate template for extreme star-bursting galaxies at any redshift.

We infer the nebular physical conditions within this galaxy — parameterized as electron temperature, pressure, density, metallicity, and ionization parameter — using widely used rest-frame optical diagnostics as well as rest-frame UV diagnostics that have been developed for use at high redshift by *JWST*, but have not been well tested. We find that SDSS J1723+3411 has a metallicity close to solar, and a higher ionization parameter and higher ISM pressure than local star-forming galaxies of the same metallicity (Kewley et al. 2006; Thomas et al. 2019). This is similar to results for other high redshift star forming galaxies (Hainline et al. 2009; Bian et al. 2010; Liu et al. 2008; Nakajima et al. 2013; Shirazi et al. 2014a,b), and supports a picture in which the mode of star formation at cosmic noon was quite different than how stars form in the local universe (e.g. Rigby et al. 2008; Rujopakarn et al. 2012).

We measure dramatically higher (1.5 dex) pressure in SDSS J1723+3411 from the rest-frame UV [C III] 1907, C III] 1909 Å diagnostic compared to the [O II] 3727, 3729 Å doublet ratio. A19 found the same offset in a lensed galaxy at $z = 1.70$. While to be expected given that [C III] 1907, C III] 1909 Å arises from hotter nebular regions than the [O II] 3727, 3729 Å (Kewley et al. 2019a), these results should be a sobering caution against inter-comparing pressures derived from the UV versus the optical diagnostics. If care is not taken, high-redshift galaxies may look more extreme than local galaxies *simply because of the diagnostics used.*

We find that the rest-frame optical strong-line diagnostics N2O2a, N2, and R23 provide consistent metallicity estimates. This is consistent with the good performance of R23 and N2 seen by Patricio et al. (2018) when comparing to the [O III] 4363 Å auroral line method; they did not examine N2O2a. In SDSS J1723+3411, we do not see an offset in the metallicity diagnostics that use N2, as was seen by Patricio et al. (2018).

Unfortunately, we find that no currently–used diagnostic that uses only rest-frame UV emission lines is able to successfully determine the metallicity, as judged against the rest-frame optical diagnostics (N2, N2O2a, and R23). This is consistent with the results of A19 for a different lensed galaxy at $z = 1.7$. The metallicity is effectively constrained for SDSS J1723+3411 using two diagnostics that incorporate [N II] 6584 Å, as well as via the electron temperature method that uses [O III] 1660,

1666 Å to [O III] 5007 Å, though with the expected offset between the electron temperature and strong-line methods.

We now consider what these results mean for *JWST* studies of galaxies at high redshift, especially at the epoch of reionization. The NIRSpec instrument's wavelength range of 0.7–5 μm can capture the following key emission lines for galaxies in a multiplexed way out to the following redshifts:

- [O III] 1660, 1666 Å for $z > 3.2$,
- [C III] 1907, C III] 1909 Å for $z > 2.7$,
- [O II] 3727, 3729 Å for $0.88 < z < 12.4$,
- [O III] 4959, 5007 Å for $0.40 < z < 9.0$, and
- Hα plus [N II] 6584 Å for $0.06 < z < 6.6$.

The metallicity diagnostics that work best for SDSS J1723+3411, which use the optical [N II] lines, will for galaxies at the reionization epoch be redshifted out of the *JWST* NIRSpec wavelength range. Indeed, this reality has fueled interest in UV–only metallicity diagnostics that would be well-suited for *JWST* studies of galaxies at the epoch of reionization. Unfortunately, given the failure of all the UV–only metallicity diagnostics (N2O2b, N3O3, Si3-O3C3, and He2-O3C3) to correctly determine the metallicity of SDSS J1723+3411 in this study, and similar results by A19, we are pessimistic about the effectiveness of these diagnostics at moderate or at high redshift. It would be timely to develop alternative rest-frame UV metallicity diagnostics, based on rest-frame UV spectral atlases at moderate redshift (for example MEGaSaURA; Rigby et al. 2018) and at low redshift, like the upcoming ULYSSES and CLASSY programs with *HST*.

In contrast to the failure of the rest-frame UV metallicity diagnostics, the electron temperature method of measuring metallicity, using the ratio of [O III] 1660,6 Å or [O III] 4363 Å to [O III] 5007 Å, has proven effective at $z \sim 1$–2 (this work, A19, and Steidel et al. 2016), and will be available to *JWST* for galaxies with redshifts below $z = 9$. Therefore, we suggest that these electron temperature diagnostics are particularly well-suited for *JWST*, with the caveat that there is a well-known offset between the electron temperature methods and the strong emission line diagnostics. We therefore suggest that *JWST* spectroscopic surveys should be sure to cover either or both of these two auroral emission lines. In addition, we suggest that *JWST* spectroscopic surveys of the epoch of reionization should invest the exposure time to capture the rest-frame optical emission lines at the red edge of NIRSpec's bandpass. In particular, based on the results of this work, we argue that NIRSpec surveys of $z \leq 9$ galaxies should capture both the [O II] 3727, 3729 Å and [O III] 4959, 5007 Å doublets. Even though this strategy requires the serial use of two gratings rather than one, we believe it is necessary to obtain reliable measurements of metallicity, pressure, and ionization parameter. As an example, for $z = 9$, the NIRSpec G235M/F170LP grating/filter pairing captures [O III] 1660, 1666 Å and [C III] 1907, C III] 1909 Å, while G395M/F290LP captures [O II] 3727, [O III] 4363, and [O III] 5007 Å. It may also make sense to obtain MIRI spectra for a subset of the survey to capture H α and [N II] 6584 Å, even though this must be one galaxy at a time. For galaxies with redshift $z > 9$, while the optical [O III] lines will not be accessible to *JWST*/NIRSpec, it would still be worth obtaining the optical [O II] lines to measure the ISM pressure.

ACKNOWLEDGMENTS

Acknowledgments: We thank Ramesh Mainali for commenting on the draft manuscript. We thank Glenn Kacprzack for assistance reducing the ESI/Keck spectra. Based on observations made with the NASA/ESA Hubble Space Telescope, obtained from the Data Archive at the Space Telescope Science Institute, which is operated by the Association of Universities for Research in Astronomy, Inc., under NASA contract NAS 5-26555. These observations are associated with program # 14230. Support for program 14230 was provided by NASA through a grant from the Space Telescope Science Institute, which is operated by the Association of Universities for Research in Astronomy, Inc., under NASA contract NAS 5-26555. Some of the data presented herein were obtained at the W.M. Keck Observatory, which is operated as a scientific partnership among the California Institute of Technology, the University of California and the National Aeronautics and Space Administration. The Observatory was made possible by the generous financial support of the W.M. Keck Foundation. We acknowledge the very significant cultural role and reverence that the summit of Maunakea has always had within the indigenous Hawaiian community. We are most fortunate to have the opportunity to conduct observations from this sacred mountain. Some of the observations reported here were obtained at the MMT Observatory, a joint facility of the University of Arizona and the Smithsonian Institution. Some of the data presented herein were obtained at the Gemini Observatory, which is operated by the Association of Universities for Research in Astronomy, Inc., under a cooperative agreement with the NSF on behalf of the Gemini partnership: the National Science Foundation (United States), the National Research Council (Canada), CONICYT (Chile), Ministerio de Ciencia, Tecnología e Innovación Productiva (Argentina), and Ministério da Ciência, Tecnologia e Inovação (Brazil).

REFERENCES

Acharyya, A., Kewley, L. J., Rigby, J. R., Bayliss, M., Bian, F., Nicholls, D., Federrath, C., Kaasinen, M., Florian, M., & Blanc, G. A. 2019, Monthly Notices of the Royal Astronomical Society, 488, 5862

Angel, J. R. P., Hilliard, R. L., & Weymann, R. J. 1979, The MMT and the Future of Ground-Based Astronomy, 385, 87

Asplund, M., Grevesse, N., Sauval, A. J., & Scott, P. 2009, Annual Review of Astronomy and Astrophysics, 47, 481

Baldwin, J. A., Phillips, M. M., & Terlevich, R. 1981, Publications of the Astronomical Society of the Pacific, 93, 5

Bayliss, M. B., Rigby, J. R., Sharon, K., Wuyts, E., Florian, M., Gladders, M. D., Johnson, T., & Oguri, M. 2014, ApJ, 790, 144

Berg, D. A., Chisholm, J., Erb, D. K., Pogge, R., Henry, A., & Olivier, G. M. 2019a, ApJ, 878, L3

Berg, D. A., Erb, D. K., Auger, M. W., Pettini, M., & Brammer, G. B. 2018, ApJ, 859, 164

Berg, D. A., Erb, D. K., Henry, R. B. C., Skillman, E. D., & McQuinn, K. B. W. 2019b, ApJ, 874, 93

Berg, D. A., Skillman, E. D., Henry, R. B. C., Erb, D. K., & Carigi, L. 2016, ApJ, 827, 126

Bian, F., Fan, X., Bechtold, J., McGreer, I. D., Just, D. W., Sand, D. J., Green, R. F., Thompson, D., Peng, C. Y., Seifert, W., Ageorges, N., Juette, M., Knierim, V., & Buschkamp, P. 2010, ApJ, 725, 1877

Bian, F., Kewley, L. J., Dopita, M. A., & Juneau, S. 2016, ApJ, 822, 62

Brammer, G. B., van Dokkum, P. G., Franx, M., Fumagalli, M., Patel, S., Rix, H.-W., Skelton, R. E., Kriek, M., Nelson, E., Schmidt, K. B., Bezanson, R., Da Cunha, E., Erb, D. K., Fan, X., Förster Schreiber, N., Illingworth, G. D., Labbé, I., Leja, J., Lundgren, B., Magee, D., Marchesini, D., Mccarthy, P., Momcheva, I., Muzzin, A., Quadri, R., Steidel, C. C., Tal, T., Wake, D., Whitaker, K. E., & Williams, A. 2012, The Astrophysical Journal Supplement, 200, 13

Brinchmann, J., Pettini, M., & Charlot, S. 2008, Monthly Notices of the Royal Astronomical Society, 385, 769

Byler, N., Dalcanton, J. J., Conroy, C., Johnson, B. D., Levesque, E. M., & Berg, D. A. 2018, ApJ, 863, 14

Byler, N., Kewley, L. J., Rigby, J. R., Acharyya, A., Berg, D. A., Bayliss, M., & Sharon, K. 2020, ApJ, 893, 1

Cardamone, C., Schawinski, K., Sarzi, M., Bamford, S. P., Bennert, N., Urry, C. M., Lintott, C., Keel, W. C., Parejko, J., Nichol, R. C., Thomas, D., Andreescu, D., Murray, P., Raddick, M. J., Slosar, A., Szalay, A., & Vandenberg, J. 2009, Monthly Notices of the Royal Astronomical Society, 399, 1191

Cardelli, J. A., Clayton, G. C., & Mathis, J. S. 1989, ApJ, 345, 245

Cox, A. N. 2000, Allen's astrophysical quantities

de Barros, S., Oesch, P. A., Labbé, I., Stefanon, M., González, V., Smit, R., Bouwens, R. J., & Illingworth, G. D. 2019, Monthly Notices of the Royal Astronomical Society, 489, 2355

Elias, J. H., Joyce, R. R., Liang, M., Muller, G. P., Hileman, E. A., & George, J. R. 2006a, Society of Photo-Optical Instrumentation Engineers (SPIE) Conference Series, 6269, 62694C

Elias, J. H., Rodgers, B., Joyce, R. R., Lazo, M., Doppmann, G., Winge, C., & Rodríguez-Ardila, A. in , SPIE Astronomical Telescopes + Instrumentation, ed. I. S. McLeanM. Iye (SPIE), 626914

Endsley, R., Stark, D. P., Chevallard, J., & Charlot, S. 2020, arXiv

Feltre, A., Charlot, S., & Gutkin, J. 2016, Monthly Notices of the Royal Astronomical Society, 456, 3354

Feltre, A., Maseda, M. V., Bacon, R., Pradeep, J., Leclercq, F., Kusakabe, H., Wisotzki, L., Hashimoto, T., Schmidt, K. B., Blaizot, J., Brinchmann, J., Boogaard, L., Cantalupo, S., Carton, D., Inami, H., Kollatschny, W., Marino, R. A., Matthee, J., Nanayakkara, T., Richard, J., Schaye, J., Tresse, L., Urrutia, T., Verhamme, A., & Weilbacher, P. M. 2020

Garnett, D. R., Shields, G. A., Skillman, E. D., Sagan, S. P., & Dufour, R. J. 1997a, ApJ, 489, 63

Garnett, D. R., Skillman, E. D., Dufour, R. J., & Shields, G. A. 1997b, ApJ, 481, 174

Gennaro, M. 2018, 1

Green, G. M., Schlafly, E. F., Finkbeiner, D. P., Rix, H.-W., Martin, N., Burgett, W., Draper, P. W., Flewelling, H., Hodapp, K., Kaiser, N., Kudritzki, R.-P., Magnier, E., Metcalfe, N., Price, P., Tonry, J., & Wainscoat, R. 2015, ApJ, 810, 25

Hainline, K. N., Shapley, A. E., Kornei, K. A., Pettini, M., Buckley-Geer, E., Allam, S. S., & Tucker, D. L. 2009, ApJ, 701, 52

Hirschmann, M., Charlot, S., Feltre, A., Naab, T., Choi, E., Ostriker, J. P., & Somerville, R. S. 2017, Monthly Notices of the Royal Astronomical Society, 472, 2468

Holden, B. P., Oesch, P. A., González, V. G., Illingworth, G. D., Labbé, I., Bouwens, R., Franx, M., van Dokkum, P., & Spitler, L. 2016, ApJ, 820, 73

Izotov, Y. I., Stasińska, G., Meynet, G., Guseva, N. G., & Thuan, T. X. 2006, Astronomy and Astrophysics, 448, 955

Jaskot, A. & Ravindranath, S. 2016

Jiang, T. 2018, Ph.D. Thesis

Jiang, T., Malhotra, S., Rhoads, J. E., & Yang, H. 2019, ApJ, 872, 145

Johnson, B. & Leja, J. 2017

Kaasinen, M., Kewley, L., Bian, F., Groves, B., Kashino, D., Silverman, J., & Kartaltepe, J. 2018, arXiv, 5568

Kennicutt, R. C. 1998, Annual Review of Astronomy and Astrophysics, 36, 189

Kewley, L. J., Dopita, M. A., Leitherer, C., Davé, R., Yuan, T., Allen, M., Groves, B., & Sutherland, R. 2013a, ApJ, 774, 100

Kewley, L. J. & Ellison, S. L. 2008, ApJ, 681, 1183

Kewley, L. J., Groves, B., Kauffmann, G., & Heckman, T. 2006, Monthly Notices of the Royal Astronomical Society, 372, 961

Kewley, L. J., Maier, C., Yabe, K., Ohta, K., Akiyama, M., Dopita, M. A., & Yuan, T. 2013b, The Astrophysical Journal Letters, 774, L10

Kewley, L. J., Nicholls, D. C., Sutherland, R., Rigby, J. R., Acharya, A., Dopita, M. A., & Bayliss, M. B. 2019a, ApJ, 880, 16

Kewley, L. J., Nicholls, D. C., & Sutherland, R. S. 2019b, Annual Review of Astronomy and Astrophysics, 57, 511

Kewley, L. J., Zahid, H. J., Geller, M. J., Dopita, M. A., Hwang, H. S., & Fabricant, D. 2015, The Astrophysical Journal Letters, 812, L20

Kinney, A. L., Bohlin, R. C., Calzetti, D., Panagia, N., & Wyse, R. F. G. 1993, Astrophysical Journal Supplement Series (ISSN 0067-0049), 86, 5

Kriek, M., van Dokkum, P. G., Franx, M., Illingworth, G. D., Coppi, P., Förster Schreiber, N. M., Gawiser, E., Labbé, I., Lira, P., Marchesini, D., Quadri, R., Rudnick, G., Taylor, E. N., Urry, C. M., & van der Werf, P. P. 2007, ApJ, 669, 776

Kubo, J. M., Allam, S. S., Drabek, E., Lin, H., Tucker, D., Buckley-Geer, E. J., Diehl, H. T., Soares-Santos, M., Hao, J., Wiesner, M., West, A., Kubik, D., Annis, J., & Frieman, J. A. 2010, ApJ, 724, L137

Labbé, I., Oesch, P. A., Bouwens, R. J., Illingworth, G. D., Magee, D., González, V., Carollo, C. M., Franx, M., Trenti, M., van Dokkum, P. G., & Stiavelli, M. 2013, ApJ, 777, L19

Liu, X., Shapley, A. E., Coil, A. L., Brinchmann, J., & Ma, C.-P. 2008, ApJ, 678, 758

López-Sánchez, Á. R., Dopita, M. A., Kewley, L. J., Zahid, H. J., Nicholls, D. C., & Scharwächter, J. 2012, Monthly Notices of the Royal Astronomical Society, 426, 2630

MacKenty, J. W. M. C. Clampin, G. G. FazioH. A. MacEwen & J. M. Oschmann (SPIE), 84421V

Markwardt, C. B. 2009, Astronomical Data Analysis Software and Systems XVIII ASP Conference Series, 411, 251

Nakajima, K., Ouchi, M., Shimasaku, K., Hashimoto, T., Ono, Y., & Lee, J. C. 2013, ApJ, 769, 3

Nakajima, K., Schaerer, D., Le Fèvre, O., Amorin, R., Talia, M., Lemaux, B. C., Tasca, L. A. M., Vanzella, E., Zamorani, G., Bardelli, S., Grazian, A., Guaita, L., Hathi, N. P., Pentericci, L., & Zucca, E. 2018, Astronomy and Astrophysics, 612, A94

Newville, M., Stensitzki, T., Allen, D. B., Rawlik, M., Ingargiola, A., & Nelson, A. 2016, Astrophysics Source Code Library

Nicholls, D. C., Kewley, L. J., & Sutherland, R. S. 2020, Publications of the Astronomical Society of the Pacific, 132, 033001

Onodera, M., Carollo, C. M., Lilly, S., Renzini, A., Arimoto, N., Capak, P., Daddi, E., Scoville, N., Tacchella, S., Tatehora, S., & Zamorani, G. 2016, ApJ, 822, 42

Patricio, V., Christensen, L., Rhodin, H., Cañameras, R., & Lara-López, M. A. 2018, Monthly Notices of the Royal Astronomical Society, 481, 3520

Peng, C. Y., Ho, L. C., Impey, C. D., & Rix, H.-W. 2010, The Astronomical Journal, 139, 2097

Pettini, M. & Pagel, B. E. J. 2004, Monthly Notices of the Royal Astronomical Society, 348, L59

Ravindranath, S., Monroe, T., Jaskot, A., Ferguson, H. C., & Tumlinson, J. 2020, ApJ, 896, 170

Rigby, J. R., Bayliss, M. B., Gladders, M. D., Sharon, K., Wuyts, E., Dahle, H., Johnson, T., & Peña-Guerrero, M. 2015, The Astrophysical Journal Letters, 814, L6

Rigby, J. R., Bayliss, M. B., Sharon, K., Gladders, M. D., Chisholm, J., Dahle, H., Johnson, T., Paterno-Mahler, R., Wuyts, E., & Kelson, D. D. 2018, The Astronomical Journal, 155, 104

Rigby, J. R., Marcillac, D., Egami, E., Rieke, G. H., Richard, J., Kneib, J.-P., Fadda, D., Willmer, C. N. A., Borys, C., van der Werf, P. P., Pérez-González, P. G., Knudsen, K. K., & Papovich, C. 2008, ApJ, 675, 262

Rigby, J. R., Wuyts, E., Gladders, M. D., Sharon, K., & Becker, G. D. 2011, ApJ, 732, 59

Rujopakarn, W., Rieke, G. H., Papovich, C. J., Weiner, B. J., Rigby, J. R., Rex, M., Bian, F., Kuhn, O. P., & Thompson, D. 2012, ApJ, 755, 168

Sanders, R. L., Shapley, A. E., Kriek, M., Reddy, N. A., Freeman, W. R., Coil, A. L., Siana, B., Mobasher, B., Shivaei, I., Price, S. H., & de Groot, L. 2016, ApJ, 816, 23

Santini, P., Fontana, A., Castellano, M., Di Criscienzo, M., Merlin, E., Amorín, R., Cullen, F., Daddi, E., Dickinson, M., Dunlop, J. S., Grazian, A., Lamastra, A., McLure, R. J., Michałowski, M. J., Pentericci, L., & Shu, X. 2017, ApJ, 847, 76

Sawicki, M. & Thompson, D. 2006, ApJ, 642, 653

Schneider, D. P., Hartig, G. F., Jannuzi, B. T., Kirhakos, S., Saxe, D. H., Weymann, R. J., Bahcall, J. N., Bergeron, J., Boksenberg, A., Sargent, W. L. W., Savage, B. D., Turnshek, D. A., & Wolfe, A. M. 1993, The Astrophysical Journal Supplement Series, 87, 45

Senchyna, P., Stark, D. P., Charlot, S., Chevallard, J., Bruzual, G., & Vidal-Garcia, A. 2020, arXiv, arXiv:2008.09780

Senchyna, P., Stark, D. P., Vidal-Garcia, A., Chevallard, J., Charlot, S., Mainali, R., Jones, T., Wofford, A., Feltre, A., & Gutkin, J. 2017, Monthly Notices of the Royal Astronomical Society, 472, 2608

Shapley, A. E., Coil, A. L., Ma, C.-P., & Bundy, K. 2005, ApJ, 635, 1006

Shapley, A. E., Reddy, N. A., Kriek, M., Freeman, W. R., Sanders, R. L., Siana, B., Coil, A. L., Mobasher, B., Shivaei, I., Price, S. H., & de Groot, L. 2015, ApJ, 801, 88

Sharon, K., Bayliss, M. B., Dahle, H., Dunham, S. J., Florian, M. K., Gladders, M. D., Johnson, T. L., Mahler, G., Paterno-Mahler, R., Rigby, J. R., Whitaker, K. E., Akhshik, M., Koester, B. P., Murray, K., Remolina González, J. D., & Wuyts, E. 2020, The Astrophysical Journal Supplement Series, 247, 12

Sheinis, A. I., Bolte, M., Epps, H. W., Kibrick, R. I., Miller, J. S., Radovan, M. V., Bigelow, B. C., & Sutin, B. M. 2002, Publications of the Astronomical Society of the Pacific, 114, 851

Shibuya, T., Ouchi, M., Harikane, Y., Rauch, M., Ono, Y., Mukae, S., Higuchi, R., Kojima, T., Yuma, S., Lee, C.-H., Furusawa, H., Konno, A., Martin, C. L., Shimasaku, K., Taniguchi, Y., Kobayashi, M. A. R., Kajisawa, M., Nagao, T., Goto, T., Kashikawa, N., Komiyama, Y., Kusakabe, H., Momose, R., Nakajima, K., Tanaka, M., & Wang, S.-Y. 2018, Publ Astron Soc Jpn Nihon Tenmon Gakkai, 70, S15

Shirazi, M., Brinchmann, J., & Rahmati, A. 2014a, ApJ, 787, 120

Shirazi, M., Vegetti, S., Nesvadba, N., Allam, S., Brinchmann, J., & Tucker, D. 2014b, Monthly Notices of the Royal Astronomical Society, 440, 2201

Stark, D. P., Auger, M., Belokurov, V., Jones, T., Robertson, B., Ellis, R. S., Sand, D. J., Moiseev, A., Eagle, W., & Myers, T. 2013, Monthly Notices of the Royal Astronomical Society, 436, 1040

Stark, D. P., Ellis, R. S., Charlot, S., Chevallard, J., Tang, M., Belli, S., Zitrin, A., Mainali, R., Gutkin, J., Vidal-Garcia, A., Bouwens, R., & Oesch, P. 2016, Monthly Notices of the Royal Astronomical Society, 464, 469

Stark, D. P., Richard, J., Siana, B., Charlot, S., Freeman, W. R., Gutkin, J., Wofford, A., Robertson, B., Amanullah, R., Watson, D., & Milvang-Jensen, B. 2014, Monthly Notices of the Royal Astronomical Society, 445, 3200

Stasińska, G. 2005, Astronomy and Astrophysics, 434, 507

Steidel, C. C., Rudie, G. C., Strom, A. L., Pettini, M., Reddy, N. A., Shapley, A. E., Trainor, R. F., Erb, D. K., Turner, M. L., Konidaris, N. P., Kulas, K. R., Mace, G., Matthews, K., & McLean, I. S. 2014, ApJ, 795, 165

Steidel, C. C., Strom, A. L., Pettini, M., Rudie, G. C., Reddy, N. A., & Trainor, R. F. 2016, ApJ, 826, 159

Storey, P. J. & Zeippen, C. J. 2000, Monthly Notices of the Royal Astronomical Society, 312, 813

Stroe, A., Sobral, D., Matthee, J., Calhau, J., & Oteo, I. 2017a, Monthly Notices of the Royal Astronomical Society, 471, 2558

—. 2017b, Monthly Notices of the Royal Astronomical Society, 471, 2575

Tang, M., Stark, D., Chevallard, J., Charlot, S., Endsley, R., & Congiu, E. 2020, arXiv, arXiv:2007.12197

Thomas, A. D., Kewley, L. J., Dopita, M. A., Groves, B. A., Hopkins, A. M., & Sutherland, R. S. 2019, ApJ, 874, 100

Tomczak, A. R., Quadri, R. F., Tran, K.-V. H., Labbé, I., Straatman, C. M. S., Papovich, C., Glazebrook, K., Allen, R., Brammer, G. B., Cowley, M., Dickinson, M., Elbaz, D., Inami, H., Kacprzak, G. G., Morrison, G. E., Nanayakkara, T., Persson, S. E., Rees, G. A., Salmon, B., Schreiber, C., Spitler, L. R., & Whitaker, K. E. 2016, ApJ, 817, 118

van Dokkum, P. G. 2001, Publications of the Astronomical Society of the Pacific, 113, 1420

Whitaker, K. E., Franx, M., Leja, J., van Dokkum, P. G., Henry, A., Skelton, R. E., Fumagalli, M., Momcheva, I. G., Brammer, G. B., Labbé, I., Nelson, E. J., & Rigby, J. R. 2014, ApJ, 795, 104

Wuyts, E., Rigby, J. R., Gladders, M. D., & Sharon, K. 2014, ApJ, 781, 61

Table 1. Fluxes for nebular emission lines in SDSS J1723+3411.

Line ID	λ_{rest}	telescope/spectrograph	$W_{r,fit}$	Δ $W_{r,fit}$	$W_{r,signi}$	flux	Δ flux	$flux_{dr}$	Δ $flux_{dr}$
O I 1304	1304.86	MMT/BC	> -5.0	-	-	< -4.9	-	< -6.0	-
O I 1306	1306.03	MMT/BC	> -5.0	-	-	< -4.7	-	< -5.8	-
Si II 1309	1309.28	MMT/BC	> -5.7	-	-	< -4.6	-	< -5.8	-
C II 1335a	1334.58	MMT/BC	> -12	-	-	<4.1	-	<5.1	-
C II 1335b	1335.66	MMT/BC	> -11	-	-	<4.05	-	<5.0	-
C II 1335c	1335.71	MMT/BC	> -11	-	-	<4.05	-	<5.0	-
He II 1640	1640.42	MMT/BC	-0.64	0.1	11.	6.4	1.4	7.8	1.8
O III] 1660	1660.81	MMT/BC	> -0.15	-	-	1.7^a	0.4^a	2.1	0.5
O III] 1666	1666.15	MMT/BC	-0.48	0.1	9.5	5.0	1	6.1	1.5
N III] 1750	1749.7	Keck/ESI	> -0.21	-	-	<1.0	-	<1.22	-
[Si III] 1882	1882.71	Keck/ESI	-0.71	0.08	16	7.0	0.8	8.6	1.0
Si III] 1892	1892.03	Keck/ESI	-0.36	0.08	8.3	3.5	0.7	4.3	0.9
[C III] 1906	1906.68	MMT/BC	-2.05	0.2	34	17	1.4	21.3	1.7
[C III] 1906	1906.68	Keck/ESI	-1.78	0.08	38	17.3	0.8	21.3	0.96
C III] 1908	1908.73	MMT/BC	-1.4	0.2	24	12.0	1	14.85	1.6
C III] 1908	1908.73	Keck/ESI	-1.23	0.08	27	12.0	0.8	14.8	1
N II] 2140	2139.68	MMT/BC	> -0.228	-	-	<0.73	-	<0.94	-
[O III] 2320	2321.66	Keck/ESI	> -0.163	-	-	<0.47	-	<0.59	-
C II] 2323	2324.21	Keck/ESI	> -0.162	-	-	<0.46	-	<0.58	-
C II] 2325c	2326.11	Keck/ESI	-0.86	0.2	15	5.7	1.2	7.1	1.5
C II] 2325d	2327.64	Keck/ESI	-0.22	0.1	3.9	1.4	0.9	1.8	1.1
C II] 2328	2328.84	Keck/ESI	> -0.156	-	-	<0.45	-	<0.55	-
Si II] 2335a	2335.12	Keck/ESI	> -0.157	-	-	<0.45	-	<0.55	-
Si II] 2335b	2335.32	Keck/ESI	> -0.155	-	-	<0.45	-	<0.55	-
Fe II 2365	2365.55	Keck/ESI	-0.26	0.07	7.3	1.7	0.4	2.1	0.5
Fe II 2396a	2396.15	Keck/ESI	-2.1	0.2	58	13.7	1	16.8	1
Fe II 2396b	2396.36	Keck/ESI	-0.265	0.1	7.3	1.7	0.8	2.1	1.0
[O II] 2470	2471.03	Keck/ESI	-1.19	0.1	26	7.2	0.7	8.7	0.8
Fe II 2599	2599.15	Keck/ESI	> -0.089	-	-	<0.21	-	<0.24	-
Fe II 2607	2607.87	Keck/ESI	> -0.1075	-	-	<0.25	-	<0.29	-
Fe II 2612	2612.65	Keck/ESI	-0.41	0.07	11	2.15	0.4	2.6	0.5
Fe II 2614	2614.61	Keck/ESI	> -0.11	-	-	<0.25	-	<0.29	-
Fe II 2618	2618.4	Keck/ESI	> -0.11	-	-	<0.25	-	<0.29	-
Fe II 2621	2621.19	Keck/ESI	> -0.11	-	-	<0.24	-	<0.28	-
Fe II 2622	2622.45	Keck/ESI	> -0.11	-	-	<0.25	-	<0.29	-
Fe II 2626	2626.45	Keck/ESI	-0.58	0.07	15	3.0	0.4	3.6	0.4
Fe II 2629	2629.08	Keck/ESI	> -0.11	-	-	<0.24	-	<0.28	-
Fe II 2631	2631.83	Keck/ESI	> -0.11	-	-	<0.24	-	<0.28	-
Fe II 2632	2632.11	Keck/ESI	-0.17	0.09	4.7	0.9	0.5	1.0	0.6

Table 1 *continued*

Table 1 *(continued)*

Line ID	$\lambda_{\rm rest}$	telescope/spectrograph	$W_{r,fit}$	Δ $W_{r,fit}$	$W_{r,signi}$	flux	Δ flux	$\rm flux_{dr}$	Δ $\rm flux_{dr}$
Mg II 2797	2798.76	Keck/ESI	> -0.18	-	-	<0.35	-	<0.40	-
Mg II 2797	2803.53	Keck/ESI	-0.69	0.09	9.5	3.1	0.4	3.7	0.5
He I 3187	3188.67	Keck/ESI	-1.1	0.1	21	4.15	0.5	4.8	0.5
Ne III 3342	3343.14	Keck/ESI	-0.21	0.07	3.7	0.7	0.2	0.84	0.3
S III 3721	3722.69	Keck/ESI	-0.64	0.1	8.4	1.8	0.3	2.1	0.4
[O II] 3727	3727.092	Keck/ESI	-26.9	0.3	260	76	0.7	86.2	0.84
[O II] 3727	3727.09	HST/WFC3-IR G102	-55	1	-	77	2	87.5	2
[O II] 3729	3729.900	Keck/ESI	-37.8	0.2	350	107	0.7	121.0	0.8
[O II] 3729	3729.88	HST/WFC3-IR G102	$-75.$	2	-	106	2	120.	3
Hη	3836.48	Keck/ESI	-2.1	0.1	25	5.5	0.35	6.2	0.4
[Ne III] 3869	3869.86	HST/WFC3-IR G102	-33	4	-	52	6	59	7
Hζ; He I	3890.15	HST/WFC3-IR G102	-13	5	-	20.	8	23	8.5
[Ne III] 3968	3968.59	HST/WFC3-IR G102	-10	1	-	17	2	18.7	2
Hϵ	3971.2	HST/WFC3-IR G102	-7.4	2.5	-	12	4	13.4	5
He I 4025; He II	4025	HST/WFC3-IR G102	-5.1	2	-	8	4	9.2	4
Hδ	4102.89	HST/WFC3-IR G102	-16.5	2	-	26.	4	29	4
Hγ	4341.68	HST/WFC3-IR G102	-43	3	-	64	5	71	6
O III 4363	4364.44	HST/WFC3-IR G102	-1.9	4	-	2.8	6	3.1	7
He I 4471	4472.7	HST/WFC3-IR G102	-3.9	3	-	5.4	4	6.0	4.2
He II 4685	4687.02	HST/WFC3-IR G102	-3.1	3	-	4	4	4.3	4.2
[Ar IV] 4741	4741.45	HST/WFC3-IR G102	-3.5	3	-	4.	4	4.8	4
Hβ	4862.68	HST/WFC3-IR G102	-119	3	-	142	4	156	5
[O III] 4959	4960.3	HST/WFC3-IR G141	-220	2	-	258	4	282	4
[O III] 5007	5008.24	HST/WFC3-IR G141	-690	6	-	776	11	849	12
He I 5875	5877.59	HST/WFC3-IR G141	-14	8	-	13	7.5	14	8
O I 6300; S III 6312	6310	HST/WFC3-IR G141	-4.0	10	-	3.1	8	3.3	8
N II 6549	6549.85	HST/WFC3-IR G141	-12.5	0.2	-	8.5	0.2	9.1	0.2
Hα	6564.61	HST/WFC3-IR G141	-624	12	-	421	8	449	8
[N II] 6584	6585.28	HST/WFC3-IR G141	-39	1	-	26.1	0.5	27.85	0.5
[S II] 6717; S II 6731	6718+6732	HST/WFC3-IR G141	-63	13	-	38	8	40	9

NOTE— Columns are: 1) line identification ; 2) rest-frame vacuum wavelength (Å); 3) which telescope and spectrograph was used to make the measurement. "BC" stands for the Blue Channel spectrograph. For *HST* we also list which 4) $W_{r,fit}$, the best-fit rest-frame equivalent width (in Å), with the sign convention that negative equivalent width indicates emission, and positive indicates absorption. 5) corresponding uncertainty on 4); 6) significance of the emission line detection; 7) observed emission line flux, in units of 10^{-17} erg s^{-1} cm^{-2}; 8) corresponding uncertainty on 7), same units; 9) dereddened emission line flux, same units, assuming a Cardelli et al. (1989) extinction law; 10) corresponding uncertainty on 9), same units. For the cases of the [O II] 3727, 3729 Å and the [C III] 1907, C III] 1909 Å, fluxes are reported from each of the two spectrographs that observed them.

[a] For the [O III] 1660, 1666 Å doublet, the 1666 Å line is detected in the MMT spectrum while the 1660 Å line is not. Since the line ratio is set by atomic physics, we infer a line flux for the 1660 Å line based on the flux of the 1666 Å line.

Table 2. Measured Balmer line ratios and inferred $E(B-V)$ reddening for SDSS J1723+3411.

line ratio	grism(s)	value	σ	inferred E(B-V)	σ
		both rolls			
Hα/Hβ	G141/G102	2.96	0.1	0.028	0.04
Hα/Hβ	G141	3.73	0.2	0.26	0.06
Hβ/Hγ	G102	2.24	0.2	0.09	0.2
Hβ/Hδ	G102	5.48	0.8	0.45	0.2
		308° roll			
Hα/Hβ	G141/G102	2.86	0.1	-0.007	0.04
Hα/Hβ	G141	3.37	0.2	0.16	0.07
Hβ/Hγ	G102	2.36	0.3	0.2	0.2
Hβ/Hδ	G102	5.16	0.8	0.4	0.2
		139° roll			
Hα/Hβ	G141/G102	2.86	0.1	-0.006	0.05
Hα/Hβ	G141	3.11	0.2	0.08	0.06
Hβ/Hγ	G102	1.98	0.2	-0.15	0.2
Hβ/Hδ	G102	5.18	1.0	0.4	0.25

NOTE— We report values from the summed grism spectra as well as from summed spectra from each roll angle. In most cases, both lines in a ratio were measured in a single grism, indicated in the "grism(s)" column; an exception is Hα/Hβ, where the more reliable measurement of the ratio takes the Hα flux from the G141 grism and the Hβ flux from the G102 grism. Uncertainties are given in the columns marked σ. The intrinsic ratios used to calculate the reddening are from an isobaric, MAPPINGS-V photoionization model that assumes spherical geometry and $\log(\mathrm{P}/k) = 6$, $\log(\mathrm{q}) = 8$ and $\log(\mathrm{O}/H) + 12 = 8.53$.

Table 3. Description of emission-line diagnostics used, for each set of physical conditions

Diagnostic	Line ratio used	Reference
	Electron temperature T_e	
Te_O3b	[O III]λ5007/O III]$\lambda\lambda$ 1660,6	Nicholls et al. (2020)
Te_O3a_I06	[O III] $\lambda\lambda$4959,5007 / [O III] λ4363	Izotov et al. (2006)
Te_O3a_N20	[O III]$\lambda\lambda$5007/[O III]λ4363	Nicholls et al. (2020)
	Density n_e or Pressure $\log(P/k)$	
C3	[C III]λ1908/[C III]λ1906	Kewley et al. (2019a)
O2	[O II]λ3729/[O II]λ3727	"
	Metallicity 12+log (O/H)	
Te_O3b_O32 (direct method)	Te_O3b ratios (as above), [O III]$\lambda\lambda$4959,5007/Hβ, and [O II]$\lambda\lambda$3727,9/Hβ	Izotov et al. (2006)
N2O2b	[N II]λ2140/[O II]λ2470	Kewley et al. (2019b)
N3O3	[N III]λ1750/[O III]$\lambda\lambda$1660,1666	"
R23	([O II]λ3727,9+[O III]$\lambda\lambda$4959,5007)/Hβ	"
N2	[N II]λ6584/Hα	"
N2O2a	[N II]λ6584/[O II]$\lambda\lambda$3727,3729	"
Si3-O3C3	Si III 1883/[C III]λ1906,8 and [O III] 1666/[C III]λ1906,8	Byler et al. (2020)
He2-O3C3	He II 1640/[C III]λ1906,8 and [O III] 1666/[C III]λ1906,8	Byler et al. (2020)
	Ionization paramater $\log(q)$ or $\log(U)$	
O32b	[O III]$\lambda\lambda$1660,6/[O II]λ2470a,b	"
C32b	[C III]$\lambda\lambda$1906,8,8/[C II]λ2323-8	"
O32a	[O III]λ5007/[O II]$\lambda\lambda$3727,9	"
Ne3O2	[Ne III]λ 3869/[O II]$\lambda\lambda$3727,9	"

UV diagnostics			Optical diagnostics		
Diagnostics	Measured values		Diagnostics	Measured values	
Electron temperature, $\times 10^4$ K					
O3b	$1.07\ ^{+0.05}_{-0.05}$		O3a_I06	$1.03\ ^{+0.27}_{-0.27}$	
-	-		O3a_N20	$1.03\ ^{+0.27}_{-0.27}$	
ISM pressure, $\log P/k$ (K/cm^3)					
C3	$7.63\ ^{+0.37}_{-0.52}$		O2	$6.02\ ^{+0.15}_{-0.34}$	
Oxygen abundance, 12+log (O/H)					
	For $\log(P/k)=6$	For $\log(P/k)=7$		For $\log(P/k)=6$	For $\log(P/k)=7$
Direct(Te_O3b_O32)	$8.30\ ^{+0.05}_{-0.05}$	$8.30\ ^{+0.05}_{-0.05}$	R23	$8.4\ ^{+0.1}_{-0.1}$	$8.56\ ^{+0.02}_{-0.02}$
N2O2b	≥ 8.20	≥ 8.39	N2	$8.62\ ^{+0.01}_{-0.01}$	$8.57\ ^{+0.01}_{-0.01}$
N3O3	≥ 8.21	≥ 8.22	N2O2a	$8.62\ ^{+0.03}_{-0.03}$	$8.60\ ^{+0.03}_{-0.03}$
Si3-O3C3	8.13 ± 0.07				
He2-O3C3	7.84 ± 0.08				
Ionization parameter, $\log q$ (cm/s)					
	For $\log(P/k)=6$	For $\log(P/k)=7$	For $\log(P/k)=6$	For $\log(P/k)=7$	
O32b	$8.13\ ^{+0.11}_{-0.12}$	$8.17\ ^{+0.11}_{-0.11}$	O32a	$8.38\ ^{+0.03}_{-0.03}$	$8.29\ ^{+0.02}_{-0.02}$
C32b	≥ 8.5	≥ 8.42	Ne3O2	$8.15\ ^{+0.06}_{-0.07}$	$8.09\ ^{+0.06}_{-0.07}$
Electron density, $\log n_e$ (cm^{-3})					
C3	$3.29\ ^{+0.32}_{-0.51}$		O2	$1.67\ ^{+0.20}_{-0.27}$	

Table 4. Inferred values for physical properties, from the emission-line diagnostics.